Post-circular expansion of eccentric binary inspirals: Fourier-domain waveforms in the stationary phase approximation

Nicolas Yunes,[1,*] K. G. Arun,[2,3,4,†] Emanuele Berti,[5,6,‡] and Clifford M. Will[2,3,§]

[1]*Department of Physics, Princeton University, Princeton, New Jersey 08544, USA*
[2]*McDonnell Center for the Space Sciences, Department of Physics, Washington University, St. Louis, Missouri 63130, USA*
[3]*GReCO, Institut d'Astrophysique de Paris, CNRS, Université Pierre et Marie Curie, 98 bis Boulevard Arago, 75014 Paris, France*
[4]*LAL, Université Paris Sud, IN2P3/CNRS, Orsay, France*
[5]*Department of Physics and Astronomy, The University of Mississippi, University, Mississippi 38677-1848, USA*
[6]*Theoretical Astrophysics 130-33, California Institute of Technology, Pasadena, California 91125, USA*
(Received 1 June 2009; published 1 October 2009)

We lay the foundations for the construction of analytic expressions for Fourier-domain gravitational waveforms produced by eccentric, inspiraling compact binaries in a post-circular or small-eccentricity approximation. The time-dependent, ''plus'' and ''cross'' polarizations are expanded in Bessel functions, which are then self-consistently reexpanded in a power series about zero initial eccentricity to eighth order. The stationary-phase approximation is then employed to obtain explicit analytic expressions for the Fourier transform of the post-circular expanded, time-domain signal. We exemplify this framework by considering Newtonian-accurate waveforms, which in the post-circular scheme give rise to higher harmonics of the orbital phase and to amplitude corrections of the Fourier-domain waveform. Such higher harmonics lead to an effective increase in the inspiral mass reach of a detector as a function of the binary's eccentricity e_0 at the time when the binary enters the detector sensitivity band. Using the largest initial eccentricity allowed by our approximations ($e_0 < 0.4$), the mass reach is found to be enhanced up to factors of approximately 5 relative to that of circular binaries for Advanced LIGO, LISA, and the proposed Einstein Telescope at a signal-to-noise ratio of ten. A post-Newtonian generalization of the post-circular scheme is also discussed, which holds the promise to provide ''ready-to-use'' Fourier-domain waveforms for data analysis of eccentric inspirals.

DOI: 10.1103/PhysRevD.80.084001 PACS numbers: 04.30.−w, 04.25.Nx, 04.30.Db, 04.30.Tv

I. INTRODUCTION

The detection and characterization of gravitational waves (GWs) hold the promise to reveal previously unattainable, yet very valuable astrophysical information (see [1] for a recent review). Ground-based detectors, such as the Laser Interferometer Gravitational Wave Observatory (LIGO) [2], VIRGO [3], GEO [4], and TAMA [5], have started acquiring data at or near design sensitivity. The space-borne Laser Interferometer Space Antenna (LISA) [6] may be launched within the next decade, while future Earth-based third-generation detectors, such as the proposed Einstein Telescope (ET) [7], are currently being planned. These detectors are expected to observe several different astrophysical GW sources, one of the most promising of which are compact binary inspirals.

Black hole (BH) binaries are considered one of the main targets for GW detection and their evolution can be roughly divided into an inspiral phase and a merger plus ringdown phase. Peters and Mathews showed that eccentric inspirals circularize via GW emission [8,9], and thus, it was traditionally thought that eccentricity would not play a major role in GW detection and analysis. One can show, for example, that to leading order $e/e_0 \sim (f/f_0)^{-19/18}$ [10], which implies that if a binary enters the sensitivity band of a ground-based interferometer at 20 Hz with an initial eccentricity of 0.1, its eccentricity is reduced to 0.01 before the system reaches 200 Hz. Circularization via GW emission, however, is not absolute, since systems that enter a detector's sensitivity band with large enough eccentricity can retain some residual eccentricity before they merge or exit the band. For example, if a binary enters the sensitivity band at 20 Hz with an initial eccentricity of 0.4, its eccentricity remains significant while in band, and is reduced to 0.01 only by the time the frequency reaches 10^3 Hz.

Astrophysical scenarios have been proposed that predict that binary inspiral signals could enter the sensitivity band of GW detectors with non-negligible eccentricity. Earth-based detectors are expected to be sensitive to stellar mass BH/BH binaries, which might fail to completely circularize before merger, leading to potentially large eccentricities in the detector band [11,12]. Wen [11] studied the evolution of the inner binary of triple BH systems in globular clusters. She found that approximately 30% of these binaries could merge via the Kozai mechanism with eccentricities ≥ 0.1 by the time they enter the LIGO band at frequency $\simeq 10$ Hz. O'Leary, Kocsis, and Loeb [12] studied the density cusp of stellar mass BHs that forms

*nyunes@princeton.edu
†arun@physics.wustl.edu
‡berti@phy.olemiss.edu
§cmw@wuphys.wustl.edu

around supermassive BHs in galactic nuclei because of mass segregation. They found that, in such dense environments, hyperbolic BH-BH encounters can lead to the formation of bound systems, and that most of these binaries ($\simeq 90\%$) would have eccentricity ≥ 0.9 when they enter the LIGO band. Several classes of compact binary sources for LISA are also predicted to be eccentric when they enter the detector's band. In order to improve readability of this paper, we have relegated a brief review of these astrophysical scenarios to Appendix A.

For binaries with non-negligible eccentricities, a dedicated search using matched-filtering techniques and eccentric orbit templates would be necessary for detection and extraction of astrophysical information. Until now, however, closed-form analytic expressions for such templates have been lacking, with most studies concentrating on the circular case. The modeling of eccentric orbits is much more difficult, since it requires knowledge not only of the orbital phase and frequency, but also of frequencies associated with the higher harmonics of the eccentric motion, as well as of frequencies associated with post-Newtonian (PN) precession effects, such as pericenter precession.

Peters and Mathews' seminal work [13], and Peters' follow-up calculation of the angular momentum flux and evolution of orbital elements at Newtonian order [9], laid the foundations for the calculation of energy and angular momentum fluxes at higher PN orders [14–21], the latter mostly focusing on circular orbits. Analytic GW templates for circular binaries are now available at 3.5PN order in the phase [22–24] and 3PN order in the amplitude [25–28], and their associated Fourier transforms have been computed in the stationary-phase approximation. Recently Ref. [29] provided a method to construct high accuracy templates for elliptical binaries in the *time domain* by explicitly computing the post-adiabatic short period contributions at 2.5PN order, to be added to the post-Newtonian expressions for the GW polarizations. A 3.5PN generalization of these templates was discussed in Ref. [30].

Relatively few investigations of data analysis issues for eccentric inspirals have been performed. Martel and Poisson [31] quantified the accuracy to which circular-orbit templates could capture signals from eccentric binaries in the LIGO band, finding that the signal-to-noise ratio (SNR) loss is significant for eccentricities above 0.1. Seto [32] studied parameter estimation in the context of eccentric galactic neutron star binaries, and Benacquista [33,34] carried out the first statistical investigation of the harmonic structure of eccentric binary waveforms and their relevance for LISA GW detection. The analysis by Martel and Poisson was recently revisited [35,36], emphasizing the need for eccentric binary templates. All these investigations, however, concentrated on either time-domain waveforms or numerical Fourier transforms of such waveforms, which might not be desirable for data analysis purposes.

The aim of this paper is to lay the foundations of a post-circular approximation that allows for the construction of analytic, ''ready-to-use'' Fourier-domain waveforms for eccentric binary inspirals. This approximation consists of expanding time-domain gravitational waveforms in the eccentricity parameter e_0, which is defined to be the eccentricity when the GW signal enters the detector sensitivity band. The resulting expression is then Fourier transformed in the stationary-phase approximation. This scheme is an extension of the program initiated by Krolak, Kokkotas and Schäfer several years ago [37] and it is intended to supplement the PN approximation, thus yielding a double or *bivariate* expansion in both the velocity of the binary members and the initial eccentricity. Although the PN scheme does not require the post-circular approximation for the construction of numerical Fourier-domain templates, closed-form analytic expressions for these templates can only be obtained through the incorporation of the post-circular approximation.

The usefulness of ready-to-use, analytic, frequency-domain waveforms is twofold. Analytic expressions allow us to study the structure of the eccentricity-induced corrections to the Fourier transform of the signal; in turn, this structure allows us to explain features in the SNR that would otherwise be hidden by numerics. Second, analytic expressions allow for fast implementations of dedicated matched-filtering searches in a data analysis algorithm and allow us to sidestep fast Fourier transforms, which would drain numerical resources from Fourier-domain data analysis pipelines.

We exemplify the post-circular approximation by considering Newtonian expressions for the two GW polarization states of elliptic binaries. The cosines and sines of the GW phase are expanded in a truncated Bessel series, whose argument is proportional to the eccentricity parameter. We find that the first 9 terms in the sum suffice to approximate the phase to better than 0.1% for eccentricities smaller than 0.4 (see Sec. II below). The Bessel series is then reexpanded to eighth order in $e \ll 1$, which we find sufficient to capture the essential features of orbital dynamics for such small eccentricities.

The structure of the time-domain gravitational waveform for eccentric inspirals takes the form

$$h_{+,\times} \sim F^{2/3} \sum_{\ell=1}^{10} [C^{(\ell)}_{+,\times} \cos(\ell l) + S^{(\ell)}_{+,\times} \sin(\ell l)], \qquad (1.1)$$

where F is the orbital frequency, l is the mean anomaly and $C_{+,\times}$ and $S_{+,\times}$ are eighth-order power series in the eccentricity [see Eqs. (3.7), (3.8), (3.9), and (3.10) and Eqs. (B1)–(B36)]. The eccentricity is itself a function of the orbital frequency, which we invert in the limit $e \ll 1$ and insert into the time-domain waveforms to obtain explicit expressions whose only independent variables are the orbital frequency and the mean anomaly. The prescription described above to compute time-domain waveforms is a completion of the analytic work of Moreno-Garrido, Buitrago and Mediavilla [38,39], improved through the

resummation methods of Pierro *et al.* [40,41] and the more general waveform expressions of Martel and Poisson [31].

Once closed-form, analytic expressions for the time-domain waveforms are obtained, we compute their Fourier transform in the stationary-phase approximation (SPA). This approximation derives from the asymptotic method of integration by steepest descent, which allows one to systematically include higher harmonics in the frequency-domain waveforms. This higher-harmonic structure is found to fit perfectly in the formalism of Refs. [42,43], which was developed to account for higher harmonics due to PN amplitude corrections in circular-orbit binary waveforms.

The Fourier transform of the response function is then found to take the form

$$\tilde{h} \sim \tilde{\mathcal{A}} f^{-7/6} \sum_{\ell=1}^{10} \left(\frac{\ell}{2}\right)^{2/3} \xi_\ell e^{-i\psi_\ell}, \tag{1.2}$$

where $\tilde{\mathcal{A}}$ is an overall amplitude that depends on the system parameters (such as the masses of the binary members), while f is the dominant (quadrupole) GW frequency. The amplitudes ξ_ℓ and the phases ψ_ℓ are small-eccentricity expansions [see Eqs. (4.28) and (C1)]. The ξ_ℓ's depend on the antenna pattern functions $F_{+,\times}$ [44], the initial eccentricity e_0 and the GW frequency. The expansion of the phase reads

$$\psi_\ell \sim -\frac{3}{128} f^{-5/3} \left(\frac{\ell}{2}\right)^{8/3} \left[1 - \frac{2355}{1462} e_0^2 \left(\frac{f}{f_0}\right)^{-19/9} + \cdots\right], \tag{1.3}$$

where f_0 is the frequency at which the eccentricity equals e_0, which we choose to coincide with the low-frequency cutoff of the detector sensitivity band. This is in agreement with the Newtonian limit of Eq. (A9) of [37] up to $\mathcal{O}(e_0^2)$.

One of the benefits of obtaining closed-form, analytic expressions for the Fourier transform of the waveforms is that its harmonic structure and its eccentricity-induced amplitude corrections become explicit. We find that these higher-harmonic eccentricity corrections increase the SNR for large total masses, in analogy to what was found for PN amplitude-corrected circular-orbit waveforms in [42,43,45]. Figure 1 compares the optimal SNR of equal-mass binaries with eccentricity $e_0 = 0$ and $e_0 = 0.3$ at the initial frequency of the sensitivity band of Advanced LIGO (AdvLIGO), ET and LISA (20, 1 or 10, and 10^{-4} Hz, respectively). The source is located at distances of 100 Mpc for AdvLIGO and ET, and 3 Gpc for LISA. By "optimal" we mean the SNR measured by an observer located in a direction perpendicular to the orbital plane (more precisely, we set $\iota = \beta = \theta_S = \phi_s = \psi_S = 0$ in the notation of Sec. III). This SNR increase is rather generic, irrespective of the location of the source in the sky.

The inclusion of eccentricity in the waveforms leads to an increase in the mass reach as compared to circular

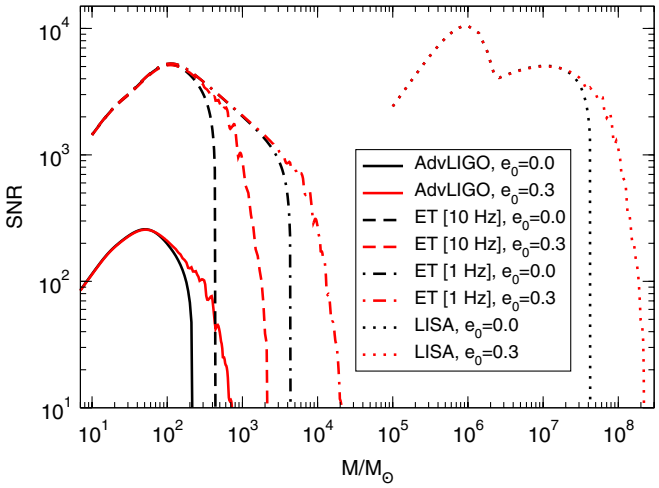

FIG. 1 (color online). SNR for an equal-mass binary at optimal orientation as a function of total mass for circular binaries and elliptic binaries with initial eccentricity of 0.3. The assumed low-frequency cutoffs for AdvLIGO, ET and LISA are 20, either 1 or 10, and 10^{-4} Hz, respectively. The sources are at 100 Mpc for AdvLIGO and ET and at 3 Gpc for LISA. The initial eccentricity corresponds to that at the low-frequency cutoff.

waveforms. This is shown in Fig. 2, where we plot the mass reach enhancement $M(e_0)/M_0$, where $M_0 = M(0)$. The mass reach $M(e_0)$ is here defined as the mass yielding an optimal SNR of ten, roughly corresponding to the largest mass visible to the detector. The mass reach usually increases with e_0, up to factors of order 5 for binaries with $e_0 \simeq 0.4$. This result should still hold when PN corrections are included, since we expect these corrections to increase the mass reach. We conclude then that LISA could potentially observe moderately eccentric binaries with total

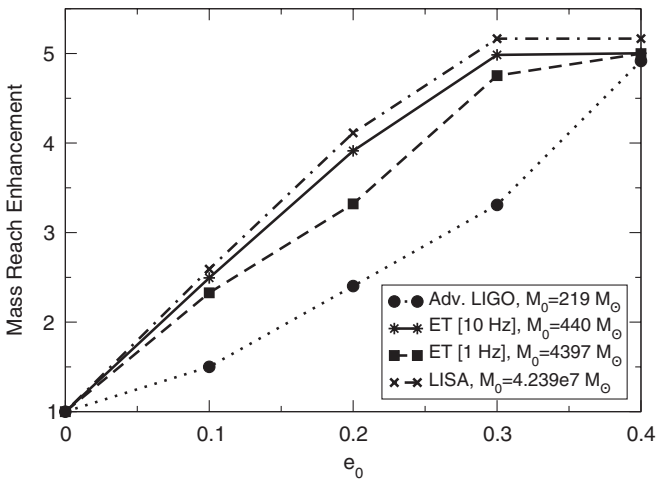

FIG. 2. Normalized mass reach enhancement, as a function of initial eccentricity. The normalization is given by the value of the mass reach for circular binaries, namely, $M_0 = 219M_\odot$, $M_0 = 440M_\odot (4397M_\odot)$ and $M_0 = 4.239 \times 10^7 M_\odot$ for AdvLIGO, ET and LISA, respectively.

masses of the order of $10^8 M_\odot$. These results are in agreement with preliminary results from numerical relativity simulations of merging eccentric binaries [46] (see also [47]).

An increase in mass reach in turn implies that, for a system of fixed total mass, the distance to which the system can be observed also increases with eccentricity. For example, intermediate-mass BH (IMBH) mergers of total mass $\simeq 200 M_\odot$ with orbital eccentricity of $e_0 \simeq 0.3$ would be observable by AdvLIGO up to approximately 1.26 Gpc ($z \simeq 0.26$) with an SNR of 10, while supermassive black holes (SMBHs) of total mass $\simeq 4 \times 10^7 M_\odot$ and initial eccentricity $e_0 \simeq 0.3$ would be visible by LISA up to approximately 100 Gpc ($z \simeq 10$) with an SNR of 100. Such an increase in distance corresponds to an increase in accessible volume of up to a factor of approximately 100 for systems with $e_0 \simeq 0.4$.

The post-circular approximation also allows us to determine how many harmonics are needed to reproduce the Fourier transform of the eccentric signal to some accuracy. For a system with $e_0 = 0.01$, we find that keeping up to the second or third harmonic suffices to reproduce the SNR of a signal that includes ten harmonics to $\mathcal{O}(1)$ and $\mathcal{O}(10^{-1})$, respectively, in the entire mass range. For a system with $e_0 = 0.1$, however, we find that a comparable accuracy in SNR requires including up to the fourth and fifth harmonic, respectively. Such an analysis allows us to conclude that the inclusion of up to the fourth harmonic suffices for SNR calculations when $e_0 \leq 0.1$, while for systems with $0.1 < e_0 \leq 0.3$, one must really include eight harmonics or more.

Although the waveforms we consider in our post-circular scheme are not accurate enough for a rigorous data analysis study, as we have ignored PN effects, they do provide insight as to the effect of eccentricity in detection and parameter estimation. As for detection, the SNRs presented here may well be smaller than SNRs for PN-corrected eccentric binary inspirals, since the addition of harmonics to the amplitudes generally increases the power in the signal. As for parameter estimation, the eccentricity corrections to the phase of the Fourier transform have a different frequency dependence relative to PN corrections to the phase in the circular case. This suggests that the initial eccentricity might be weakly correlated to other intrinsic parameters. A more detailed study is necessary to verify this conjecture, and it will be a topic for future work. In Sec. VI we outline a possible extension of the formalism to higher PN orders. When this extension is achieved, ready-to-use Fourier-domain gravitational waveforms could be employed in GW searches and parameter estimation.

The remainder of this paper deals with the details of the calculations and results presented above. It is organized as follows. Section II presents the basics of the Kepler problem and establishes the notation used in this paper. Section III discusses how to model GWs from eccentric binary inspirals in the time domain, while Sec. IV describes its frequency-domain representation. Section V presents the SNR calculation, while Sec. VI discusses PN corrections. Section VII concludes and points to future research.

Technical details are discussed in the appendixes. Appendix A reviews astrophysical scenarios that could produce eccentric binaries in the LISA band. Appendixes B and C list some lengthy coefficients appearing in our analytic calculations. Appendix D discusses the effect of possible eccentricity-induced modifications to the innermost-stable circular orbit (ISCO), concluding that they are negligible in our context. Finally, Appendix E shows how to compute the orbital frequency at some given time before merger for eccentric binaries.

In this work we follow the conventions of Misner, Thorne and Wheeler [48]. Unless otherwise specified, we use geometrical units, where $G = c = 1$, G stands for Newton's gravitational constant and c for the speed of light.

II. THE BASICS OF THE KEPLER PROBLEM

In this section, we review some of the basic concepts related to the Kepler problem in Newtonian mechanics, as they are relevant to this paper. We present here only a minimal description of this problem and refer the reader to [49] for a more detailed account. We also establish the notation we shall employ in the remainder of this paper.

Consider a system of two point particles in an eccentric orbit. In the Newtonian Keplerian representation, the Newtonian orbital trajectories are given by

$$r = a(1 - e\cos u), \tag{2.1}$$

$$N(t - t_0) = l = u - e\sin u, \tag{2.2}$$

$$\phi - \phi_0 = \upsilon \equiv 2\arctan\left[\left(\frac{1+e}{1-e}\right)^{1/2}\tan\frac{u}{2}\right], \tag{2.3}$$

where the notation, following [50], is as follows: ϕ is the orbital phase; $\vec{r}$ is the relative separation vector between the compact objects, namely, $\vec{r} = r(\cos\phi, \sin\phi, 0)$; a is the semimajor axis of the ellipse; e is the eccentricity parameter; u is the eccentric anomaly; l is the mean anomaly; υ is the true anomaly; and N is the mean motion. The quantities t_0 and ϕ_0 are some initial time and initial orbital phase that arise as constants of integration. Since the energy and angular momentum fluxes depend on a and e, and together cause the latter to vary with time, it can be shown that a and e coevolve according to [8,9]

$$a(e) = \left(\frac{M}{4\pi^2 F^2}\right)^{1/3} = c_0 \sigma(e), \tag{2.4}$$

where $M = m_1 + m_2$ is the total mass. The quantity F is the Keplerian mean orbital frequency, which can be associated with an instantaneous mean orbital frequency whose

evolution is discuss further in Sec. IV B. The quantity c_0 is a constant defined by $F(e_0) = F_0$ and the function $\sigma(e)$ is given by

$$\sigma(e) = \frac{e^{12/19}}{(1-e^2)}\left[1 + \frac{121}{304}e^2\right]^{870/2299}. \tag{2.5}$$

The quantity e_0 is henceforth always defined to be the eccentricity when the GW signal enters the detector sensitivity band. For AdvLIGO, ET and LISA, this corresponds to the initial eccentricity at 20, 1 or 10, and 10^{-4} Hz, respectively.

Gravitational waveforms for binary inspirals depend on trigonometric functions of the orbital phase, but for eccentric inspirals this phase is a complicated function of the orbital frequency. In the circular-orbit limit ($e \to 0$), the orbital phase satisfies $\phi = 2\pi F(t)(t - t_0)$, where F is the Keplerian orbital frequency (one-half the dominant, quadrupole GW frequency). For eccentric inspirals, however, the phase is related to the arctangent of the eccentric anomaly, which is then related in a transcendental way to the mean motion, and thus, to the frequency $N = 2\pi F$. We must then find a way to express the orbital phase as a function of the mean anomaly l.

Let us reexpress the cosine and sine of the orbital phase in terms of the mean anomaly, through the well-known Keplerian relations [40]

$$\frac{r}{a}\cos\phi = \cos u - e, \tag{2.6}$$

$$\frac{r}{a}\sin\phi = (1-e^2)^{1/2}\sin u. \tag{2.7}$$

Equation (2.1) allows us to rewrite these relations as

$$\cos\phi = \frac{\cos u - e}{1 - e\cos u}, \tag{2.8}$$

$$\sin\phi = (1-e^2)^{1/2}\frac{\sin u}{1 - e\cos u}. \tag{2.9}$$

Moreover, from the Fourier analysis of the Kepler problem, one can expand trigonometric functions of the eccentric anomaly as series of Bessel functions of the first kind, J_k. One then finds that [40]

$$\frac{\sin u}{1 - e\cos u} = 2\sum_{k=1}^{\infty} J_k'(ke)\sin kl, \tag{2.10}$$

$$\frac{\cos u}{1 - e\cos u} = \frac{2}{e}\sum_{k=1}^{\infty} J_k(ke)\cos kl, \tag{2.11}$$

where primes stand for derivatives with respect to the argument, and

$$J_k(y) \equiv \sum_{m=0}^{\infty}\frac{(-1)^m}{m!\Gamma(m+k+1)}\left(\frac{y}{2}\right)^{2m+k}, \tag{2.12}$$

with Γ the Gamma function (see e.g. [51]).

With these relations, we can now express the cosine and sine of the orbital phase as a function of the mean anomaly. Inserting Eqs. (2.10) and (2.11) into Eqs. (2.8) and (2.9) we find that

$$\cos\phi = -e + \frac{2}{e}(1-e^2)\sum_{k=1}^{\infty} J_k(ke)\cos kl, \tag{2.13}$$

$$\sin\phi = (1-e^2)^{1/2}\sum_{k=1}^{\infty}[J_{k-1}(ke) - J_{k+1}(ke)]\sin kl. \tag{2.14}$$

Equations (2.13) and (2.14) agree with the corresponding expressions in the appendix of Ref. [38]. These relations allow us to express the gravitational waveforms for eccentric inspirals as explicit functions of the orbital frequency.

The number of terms we should keep in the Bessel function expansion depends on the desired accuracy relative to the exact solution, as well as on the magnitude of the eccentricity. Figure 3 plots the numerical solution of Eq. (2.8) for the sine of the orbital phase with an eccentricity of 0.99, together with the Bessel expansion of the solution given in Eq. (2.14), where we keep 3 (dotted line), 7 (dashed line), 10 (dotted-dashed line) and 15 (dotted-dotted-dashed line) terms in the sum. Observe that even for such large eccentricities we only need fewer than 10 terms to reproduce the exact solution quite accurately.

The number of terms needed to reproduce the exact solution does depend on the eccentricity one is trying to model. As an example, consider solving Eq. (2.2) for the sine of the eccentric anomaly both numerically and with Bessel functions. The latter solution is simply given by [40]

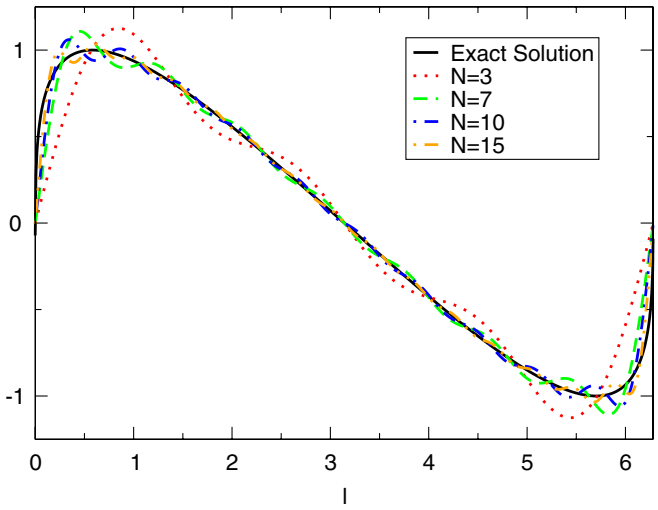

FIG. 3 (color online). Plot of the sine of the phase calculated numerically (solid black line) and expanded in Bessel functions for a system with $e_0 = 0.99$, following Eq. (2.14), and keeping 3 (dotted red line), 7 (dashed green line), 10 (dotted-dashed blue line) and 15 (dotted-dotted-dashed orange line) terms.

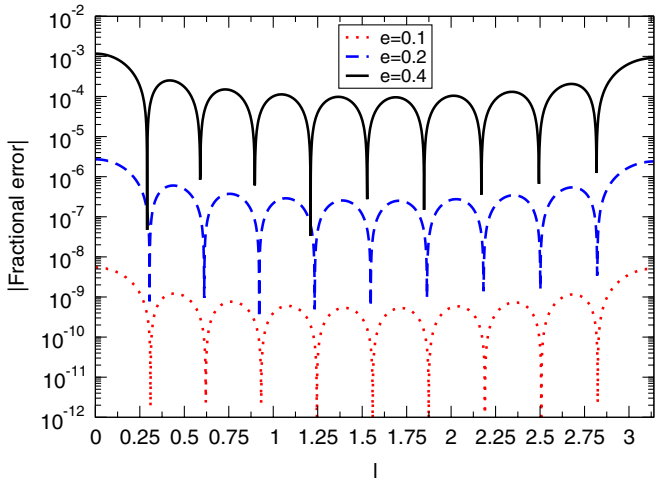

FIG. 4 (color online). Plot of the absolute value of the fractional relative difference between the sine of the eccentric anomaly, calculated numerically and expanded in Bessel functions with 9 terms, for different eccentricities ($e = 0.4$ solid black curve, $e = 0.2$ blue dashed curve, and $e = 0.1$ red dotted curve). The results are here normalized by the exact numerical solution.

$$\sin u = \frac{2}{e}\sum_{k=1}^{\infty} J_k(ke)\frac{\sin kl}{k}. \tag{2.15}$$

In Fig. 4 we plot the absolute value of the fractional relative difference between the numerical solution and the Bessel-expanded solution, keeping 9 terms in the sum. We plot the absolute value of the difference, normalized by the numerical solution for different eccentricities: $e = 0.1$ in dotted red, $e = 0.2$ in dashed blue, and $e = 0.4$ in solid black. Observe that the error due to neglecting terms beyond the 9th in the sum amount to less than 0.1% in the worst case (corresponding to the highest eccentricity $e = 0.4$). For cases with smaller eccentricity, such as $e = 0.2$ and $e = 0.1$, the relative fractional error is always much smaller (10^{-5} and 10^{-8} for the examples above, respectively).

The small-eccentricity assumption could be removed by working directly with the full series in Eqs. (2.13) and (2.14), or by resumming it. In fact, Pierro *et al.* [40] have shown how to sum the infinite Bessel series to measure the so-called "total harmonic distortion," which is loosely related to Apostolatos' fitting factor [52]. We shall not, however, work with such resummations here, since we shall be interested in binaries with eccentricities $e < 0.4$. In view of this, we shall truncate all expressions at order 10 in the Bessel expansions.

III. POST-CIRCULAR EXPANSION OF TIME-DOMAIN ECCENTRIC INSPIRAL WAVEFORMS

In this section we describe how to model gravitational radiation from eccentric inspiraling binaries in the time domain. We shall employ the quadrupole formalism, similar to that presented by Moreno-Garrido, Buitrago and Mediavilla [38,39], but improved through the techniques introduced by Pierro *et al.* [40,41].

The starting point is the expression for plus- and cross-polarized gravitational waveforms h_+ and $h_\times$, respectively. We place the GW detector at luminosity distance D_L from the source, in a direction characterized by the polar angles ι and β, defined as those subtended by the local Cartesian reference frame of the source and the line of sight vector [31]. Following Martel and Poisson [31], we rewrite the expressions of Wahlquist [53] as follows:

$$\begin{aligned} h_+ &= -\frac{\mu}{pD_L}\Big\{\Big[2\cos(2\phi - 2\beta) + \frac{5e}{2}\cos(\phi - 2\beta) \\ &\quad + \frac{e}{2}\cos(3\phi - 2\beta) + e^2\cos(2\beta)\Big](1 + \cos^2\iota) \\ &\quad + [e\cos\phi + e^2]\sin^2\iota\Big\}, \\ h_\times &= -\frac{\mu}{pD_L}[4\sin(2\phi - 2\beta) + 5e\sin(\phi - 2\beta) \\ &\quad + e\sin(3\phi - 2\beta) - 2e^2\sin(2\beta)]\cos\iota, \end{aligned} \tag{3.1}$$

where $\mu = m_1 m_2/M$ is the reduced mass, D_L is the luminosity distance, ϕ is the same orbital phase presented in Eq. (2.3) and p is the semilatus rectum, which is related to the orbital frequency via Kepler's second law

$$\frac{1}{F} = 2\pi M^{-1/2}\left(\frac{p}{1 - e^2}\right)^{3/2}. \tag{3.2}$$

GWs are clearly dominated, at least for small eccentricities, by components oscillating at 1, 2 and 3 times the orbital frequency. Equation (3.1) is valid in the quadrupole approximation, which means that higher multipoles (the octupole, hexadecapole and higher) have been neglected. These multipoles are proportional to terms of $\mathcal{O}(\dot{r}/c)$ and higher, which implies that Eq. (3.1) is a good approximation for slow velocities and weak gravity.

The harmonic structure discussed above can be seen more clearly if we reexpress Eq. (3.1), by using trigonometric identities, as

$$\begin{aligned} h_+ &= \frac{\mathcal{A}}{1 - e^2}\Big\{\cos\phi\Big[es_i^2 + \frac{5e}{2}c_{2\beta}(1 + c_i^2)\Big] \\ &\quad + \sin\phi\Big[\frac{5e}{2}s_{2\beta}(1 + c_i^2)\Big] + \cos2\phi[2c_{2\beta}(1 + c_i^2)] \\ &\quad + \sin2\phi[2s_{2\beta}(1 + c_i^2)] + \cos3\phi\Big[\frac{e}{2}c_{2\beta}(1 + c_i^2)\Big] \\ &\quad + \sin3\phi\Big[\frac{e}{2}s_{2\beta}(1 + c_i^2)\Big] + e^2s_i^2 + e^2(1 + c_i^2)c_{2\beta}\Big\}, \end{aligned} \tag{3.3}$$

$$h_\times = \frac{\mathcal{A}}{1-e^2}\{\cos\phi[-5es_{2\beta}c_i] + \sin\phi[5ec_{2\beta}c_i] + \cos2\phi[-4s_{2\beta}c_i] + \sin2\phi[4c_{2\beta}c_i] + \cos3\phi[-es_{2\beta}c_i] + \sin3\phi[ec_{2\beta}c_i] - 2e^2s_{2\beta}c_i\}, \tag{3.4}$$

where we defined $c_i \equiv \cos\iota$, $s_i \equiv \sin\iota$, $c_{2\beta} \equiv \cos2\beta$ and $s_{2\beta} \equiv \sin2\beta$, and we introduced the amplitude

$$\mathcal{A} \equiv -\frac{\mathcal{M}}{D_L}(2\pi\mathcal{M}F)^{2/3}, \tag{3.5}$$

with the chirp mass given by $\mathcal{M} \equiv \mu^{3/5}M^{2/5}$. In the limit $e \ll 1$ the dominant term is the second harmonic, followed by the first and third harmonics, while the constant term contributes only to higher order.

Explicit expressions for the waveforms as functions of time are needed to construct their Fourier transform. We shall thus substitute the expansions of the sines and cosines of the phase in terms of Bessel functions [Eqs. (2.13) and (2.14)] into Eqs. (3.3) and (3.4). The Bessel functions, however, are themselves polynomials in the eccentricity, which we are also expanding about. Three different expansions are thus taking place:

(i) *PN and multipole expansion*.—Weak-field expansion of the metric in terms of mass and current multipole moments of the source distribution, which are then expanded in small velocities.

(ii) *Bessel expansion*.—Expansion of the orbital phase in Bessel coefficients.

(iii) *Eccentricity expansion*.—Expansion of Bessel coefficients in small eccentricities.

The multipolar expansion is a weak-field expansion to solutions to the Einstein equations, where we shall here keep only the mass quadrupole. This implies that our waveforms are accurate only to Newtonian order, where we neglect terms of relative order $\mathcal{O}(\dot{r}/c)$. Such terms can be accounted for through a PN analysis, as we shall discuss in Sec. VI.

The Bessel and eccentricity expansions are related, and one must ensure that they are performed to a consistent order. Bessel functions of the first kind behave as $J_k(ke) \sim e^k$ asymptotically for $e \ll 1$. The phases in Eqs. (2.13) and (2.14), however, scale as $\sin\phi \sim \cos\phi \sim J_k(ke)/e \sim e^{k-1}$. Thus, an expansion of the waveforms to $\mathcal{O}(e^N)$ requires the phases in Eqs. (2.13) and (2.14) to be summed up to $k_{\max} = N + 1$. We shall here sum up to $N = 8$, which means that the Bessel sums in Eqs. (2.13) and (2.14) must be performed up to $k_{\max} = 9$.

With these expansions, the waveforms can be written as a sum over harmonics. Using that the mean anomaly $l = 2\pi F(t - t_0)$, the waveforms become

$$h_{+,\times} = \mathcal{A}\sum_{\ell=1}^{10}[C^{(\ell)}_{+,\times}\cos(\ell l) + S^{(\ell)}_{+,\times}\sin(\ell l)], \tag{3.6}$$

where the $\ell = 1$ coefficients are

$$C^{(1)}_+ = s_i^2\left(e - \frac{1}{8}e^3 + \frac{1}{192}e^5 - \frac{1}{9216}e^7\right) + (1 + c_i^2)c_{2\beta}\left(-\frac{3}{2}e + \frac{2}{3}e^3 - \frac{37}{768}e^5 + \frac{11}{7680}e^7\right), \tag{3.7}$$

$$S^{(1)}_+ = s_{2\beta}(1 + c_i^2)\left(-\frac{3}{2}e + \frac{23}{24}e^3 + \frac{19}{256}e^5 + \frac{371}{5120}e^7\right), \tag{3.8}$$

$$C^{(1)}_\times = s_{2\beta}c_i\left(3e - \frac{4}{3}e^3 + \frac{37}{384}e^5 - \frac{11}{3840}e^7\right), \tag{3.9}$$

$$S^{(1)}_\times = c_{2\beta}c_i\left(-3e + \frac{23}{12}e^3 + \frac{19}{128}e^5 + \frac{371}{2560}e^7\right), \tag{3.10}$$

and higher-order coefficients are listed in Appendix B. This expansion resembles that of [39], but it differs in that we are here allowing for arbitrary binary inclinations via the angles (ι, β) and we are consistently expanding to the same order in eccentricity, without keeping prefactors of $(1 - e)^{-1}$. We have checked that our results in Eqs. (3.7), (3.8), (3.9), and (3.10) and those in Appendix B are consistent with Eqs. (16)–(18) of Ref. [39], after identifying their variable Θ with our ι and reexpanding their expressions in powers of e.

The maximum k that one employs in the sums of the Bessel expansion, $k_{\max}$, is not generically equal to the maximum ℓ one uses in the sums of the harmonic decomposition of the waveform, $\ell_{\max}$. This is because higher harmonics in the waveform, such as $h_{+,\times} \sim \cos3\phi$, can be reexpanded as powers of $\cos\phi$ and $\sin\phi$ with standard

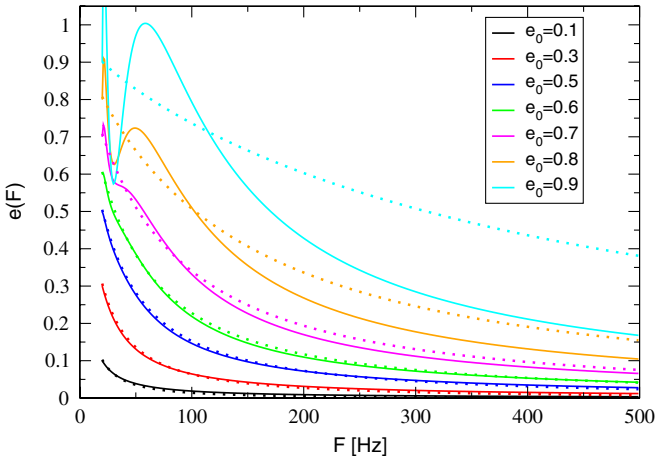

FIG. 5 (color online). Eccentricity as a function of frequency for different value of the initial eccentricity e_0 evaluated at $F_0 = 20$ Hz. Solid lines correspond to the eccentricity as given by Eq. (3.11) for $e_0 = \{0.1, 0.3, 0.5, 0.6, 0.7, 0.8, 0.9\}$, in ascending order. Dotted lines correspond to the approximant of Eq. (3.12) for the same initial eccentricities.

trigonometric identities, which then become powers of Bessel series via Eqs. (2.13) and (2.14). Cross terms in the product of Bessel series combine to produce harmonics of higher order. For example, if $k_{\max} = 4$, the harmonic decomposition contains terms of the form $h_{+,\times} \sim h_0 e^8 \cos 10l$. Increasing $k_{\max}$ leads to terms that modify h_0, but only up to $k_{\max} = 9$, beyond which h_0 is not modified. Generically, this means that $\ell_{\max} = k_{\max} + 1 = N + 2$, so with our choices ($N = 8$, $k_{\max} = 9$), we have $\ell_{\max} = 10$.

The expressions presented above depend on the eccentricity, which itself is a function of time. Equation (2.4) can be solved for the orbital frequency as a function of the eccentricity to obtain $F/F_0 = [\sigma(e_0)/\sigma(e)]^{3/2}$, where F_0 is defined such that $F(e_0) = F_0$. This equation is not invertible for large eccentricities, but in the limit $e \ll 1$ it yields

$$e \sim e_0 \chi^{-19/18}\Bigg\{1 + \frac{3323}{1824} e_0^2 [1 - \chi^{-19/9}] + \frac{15\,994\,231}{6\,653\,952} e_0^4 \Bigg[1 - \frac{66\,253\,974}{15\,994\,231}\chi^{-19/9} + \frac{50\,259\,743}{15\,994\,231}\chi^{-38/9}\Bigg] + \frac{105\,734\,339\,801}{36\,410\,425\,344} e_0^6 \Bigg[1 - \frac{1\,138\,825\,333\,323}{105\,734\,339\,801}\chi^{-19/9} + \frac{2\,505\,196\,889\,835}{105\,734\,339\,801}\chi^{-38/9} - \frac{1\,472\,105\,896\,313}{105\,734\,339\,801}\chi^{-19/3}\Bigg] + \mathcal{O}(e_0)^8\Bigg\}, \tag{3.11}$$

where we have defined $\chi \equiv F/F_0$. Notice that Eq. (3.11) is a series in odd powers of e_0, and as such, it possesses uncontrolled remainders of $\mathcal{O}(e_0^9)$.

The inversion of the eccentricity as a function of frequency is not valid for all frequencies and all initial eccentricities. Figure 5 plots Eq. (3.11) as a function of frequencies for different initial eccentricities, and initial frequency $F_0 = 20$ Hz. Observe that for initial eccentricities $e_0 \leq 0.6$, $e(F)$ decays monotonically as a function of frequency, as expected, but for $e_0 > 0.6$ it ceases to be monotonic, displaying two peaks. This unphysical behavior is a signal that the expansion in Eq. (3.11) breaks down. This occurs when the first correction in the e_0 expansion ceases to be much less than unity. This requirement translates roughly to $F \gg 1.2 e_0^{18/19} F_0$, or simply $e_0 \ll 0.8$. We see then that truncating all expressions at $e < 0.4$ is consistent with this requirement. More importantly, Fig. 5 shows that Eq. (3.11) is well-behaved for this range of eccentricities.

Monotonicity, however, is not sufficient to guarantee that Eq. (3.11) is valid up to $e = 0.4$. The ultimate test is to compare this power-series solution to the exact numerical inversion of Eq. (2.4). We find that the exact numerical solution can be fitted by the following phenomenological fraction to better than 1% accuracy:

$$e(F) = \frac{16.83 - 3.814\beta^{0.3858}}{16.04 + 8.1\beta^{1.637}}, \tag{3.12}$$

where we have defined $\beta \equiv \chi^{2/3}/\sigma(e_0)$. One can check that in the limit $\chi \to 1$, Eq. (3.12) equals e_0 with an accuracy of roughly 1%. Equation (3.12) is plotted in Fig. 5 with dotted lines. Observe that the dotted lines are always close to the solid lines for $e_0 < 0.7$. The use of Eq. (3.12), however, would go against the philosophy of this paper: to power-series expand all quantities in the limit $e_0 \ll 1$. We leave exploration of this type of resummation and others for future work.

The waveform coefficients can now be written entirely as a generalized power-series expansion in the frequency. Inserting Eq. (3.11) into Eq. (3.6) and reexpanding in the limit $e \ll 1$, we find, for example,

$$C_+^{(2)} = (1 + c_i^2) c_{2\beta}\Bigg[2 - 5e_0^2\chi^{-19/9} + \Bigg(-\frac{16\,615}{912}\chi^{-19/9} + \frac{19\,123}{912}\chi^{-38/9}\Bigg)e_0^4 + \Bigg(-\frac{8\,448\,925}{207\,936}\chi^{-19/9} + \frac{63\,545\,729}{415\,872}\chi^{-38/9} - \frac{234\,273\,299}{2\,079\,360}\chi^{-19/3}\Bigg)e_0^6 + \Bigg(-\frac{41\,434\,504\,475}{568\,912\,896}\chi^{-19/9} + \frac{469\,672\,525\,907}{758\,550\,528}\chi^{-38/9} - \frac{778\,490\,172\,577}{632\,125\,440}\chi^{-19/3} + \frac{1\,559\,384\,621\,213}{2\,275\,651\,584}\chi^{-76/9}\Bigg)e_0^8\Bigg] + s_i^2\Bigg[e_0^2\chi^{-19/9} + \Bigg(\frac{3323}{912}\chi^{-19/9} - \frac{1209}{304}\chi^{-38/9}\Bigg)e_0^4 + \Bigg(\frac{1\,689\,785}{207\,936}\chi^{-19/9} - \frac{1\,339\,169}{46\,208}\chi^{-38/9} + \frac{8\,690\,279}{415\,872}\chi^{-19/3}\Bigg)e_0^6 + \Bigg(\frac{8\,286\,900\,895}{568\,912\,896}\chi^{-19/9} - \frac{9\,897\,925\,427}{84\,283\,392}\chi^{-38/9} + \frac{28\,877\,797\,117}{126\,425\,088}\chi^{-19/3} - \frac{1\,428\,551\,432\,057}{11\,378\,257\,920}\chi^{-76/9}\Bigg)e_0^8\Bigg]. \tag{3.13}$$

Notice that in the limit $e_0 \to 0$, Eq. (3.13) reduces to the appropriate circular limit: $C_+^{(2)} \to 2(1 + c_i^2)c_{2\beta}$. As we can see, the modified coefficients are complicated and unilluminating, which is why we do not present the remaining ones here. Nonetheless, it is straightforward to insert Eq. (3.11) into the waveforms of Eq. (3.6) to obtain amplitude corrections as a function of the orbital frequency.

IV. FOURIER TRANSFORM OF THE WAVEFORM IN THE SPA

In this section we calculate the Fourier transform of the waveform computed in the previous section. To do so, we shall employ the SPA (see [54,55] for a discussion in the context of GW data analysis), which is an expansion in the ratio of the radiation-reaction time scale to the orbital period. In this asymptotic expansion we need only keep the controlling factor, since subdominant terms can in general be neglected for matched-filtering purposes [56]. Recently, it has been proposed that amplitude corrections in the waveforms might play a critical role in the data analysis problem [42,43,45,57–64], but we defer a discussion of those corrections to future work. We shall here primarily follow the prescription of [37].

Let us begin by reviewing the SPA, following Ref. [54]. Consider the generalized Fourier integral

$$I(y) = \int_a^b g(t) e^{iy\psi(t)} dt, \tag{4.1}$$

where $g(t)$, $\psi(t)$, a, b and y are all real. In order to find the asymptotic behavior of such an integral as $y \to +\infty$, one searches for *stationary* points, namely, those where $\dot{\psi} = 0$. This is because in the neighborhood of stationary points the integrand oscillates less rapidly, and there is less cancellation between adjacent subintervals [54]. Thus, the asymptotic behavior of Eq. (4.1) is given by

$$I(y) \sim g(a) e^{iy\psi(a) \pm i\pi/(2p)} \left[\frac{p!}{y|\psi^{(p)}(a)|}\right]^{1/p} \frac{\Gamma(1/p)}{p} \tag{4.2}$$

as $y \to +\infty$, where $\psi^{(p)}(a)$ stands for the pth derivative of ψ evaluated at $t = a$. In Eq. (4.2) the factor of $e^{\pm i\pi/(2p)}$ has a positive sign if $\psi^{(p)}(a) > 0$, and a negative sign if $\psi^{(p)}(a) < 0$. Here we have chosen the stationary point to be located at $t = a$, such that $\psi^{(1)}(a) = \cdots = \psi^{(p-1)}(a) = 0$.

Let us then define the Fourier transform of some time series $B(t)$ as

$$\tilde{B}(f) \equiv \int_{-\infty}^{\infty} B(t) e^{2\pi i f t} dt, \tag{4.3}$$

and let us write the time-domain waveform as the product of a slowly varying amplitude $\mathcal{A}(t)$ and a rapidly varying cosine with phase $\ell\phi(t)$ and $\ell > 0$. Then, the Fourier transform of the cosine (denoted by a subscript C) becomes

$$\tilde{B}_C(f) = \frac{1}{2} \int_{-\infty}^{\infty} \mathcal{A}(t)(e^{2\pi i f t + i\ell\phi(t)} + e^{2\pi i f t - i\ell\phi(t)}) dt. \tag{4.4}$$

The first term in Eq. (4.4) does not contain any stationary points and, thus, it vanishes via the Riemann-Lebesgue lemma [54]. The second term, however, does have a stationary point at the value t_0 where $\ell\dot{\phi}(t_0) = 2\pi f$, which defines the *stationary-phase condition*: $F(t_0) = f/\ell$, where we have defined $F(t) \equiv \dot{\phi}(t)/(2\pi)$. Thus, the asymptotic behavior of the Fourier transform of a cosine time series is

$$\tilde{B}_C(f) = \frac{\mathcal{A}(t_0)}{2\sqrt{\ell \dot{F}(t_0)}} e^{-i(\Psi + \pi/4)}, \tag{4.5}$$

where we have defined the phase

$$\Psi := -2\pi f t_0 + \ell\phi(t_0). \tag{4.6}$$

The Fourier transform of a sine times series is then simply $\tilde{B}_S(f) = i\tilde{B}_C(f)$. Equation (4.5) is identical to Eq. (4.2) with $p = 2$, $g(t) = \mathcal{A}(t)/2$, $y = f$ and $\psi(t) = 2\pi t - \ell\phi(t)/f$. In obtaining this solution we have implicitly assumed that $d(\ln\mathcal{A})/dt \ll d\phi/dt$ and $d^2\phi/dt^2 \ll (d\phi/dt)^2$, which mathematically enforces the physical condition that the amplitude varies much more slowly than the phase. In Eq. (4.5) there is an extra factor of 2 relative to Eq. (4.2), because the phase Ψ is not monotonic in its range.[1]

In order to find the full solution, we must solve for the phase Ψ. Defining the quantity $\tau \equiv F/\dot{F}$, we can rewrite $\phi(F)$ and $t(F)$ as

$$\phi(F) = 2\pi \int^F \tau' dF', \qquad t(F) = \int^F \frac{\tau'}{F'} dF', \tag{4.7}$$

which then leads to

$$\Psi[F(t_0)] = 2\pi \int^{F(t_0)} \tau' \left(\ell - \frac{f}{F'}\right) dF'. \tag{4.8}$$

Of course, these expressions must be evaluated at the stationary point, given above by $F(t_0) = f/\ell$.

A. Circular case

The above formalism can be understood better by studying the well-known circular case. Let us then solve explicitly for the Fourier transform of the response function $h(t)$ in the SPA for a binary in circular orbit ($e = 0$). The response function is defined via the linear combination

$$h(t) = F_+(\theta_S, \phi_S, \psi_S)h_+ + F_\times(\theta_S, \phi_S, \psi_S)h_\times, \tag{4.9}$$

[1]The stationary-phase integral can be broken down into two parts, inside each of which ψ is monotonic. Each of these integrals has a stationary-phase contribution that leads to the factor of 2 in Eq. (4.2). See [56] for more details.

where F_+ and $F_\times$ are the so-called beam-pattern functions that characterize the response of the detector to an impinging GW and are also slowly varying (see e.g. [65]). The orbital frequency evolution is given by

$$\frac{dF}{dt} = \frac{48}{5\pi\mathcal{M}^2}(2\pi\mathcal{M}F)^{11/3} \tag{4.10}$$

[see e.g. the leading-order contribution to Eq. (A.2) in [42]]. We can rewrite the response function of Eq. (4.9) as $h(t) = h_C(t) + h_S(t)$, where

$$h_C(t) = \mathcal{A}\,Q_C(\iota,\beta)\cos 2\phi, \tag{4.11}$$

$$h_S(t) = \mathcal{A}\,Q_S(\iota,\beta)\sin 2\phi, \tag{4.12}$$

and where the amplitude $\mathcal{A}$ is a function of frequency, defined in Eq. (3.5). We have here introduced the following functions of the polarization and inclination angles, respectively:

$$Q_C(\iota,\beta) \equiv 2(1+c_i^2)c_{2\beta}F_+ - 4c_i s_{2\beta}F_\times, \tag{4.13a}$$

$$Q_S(\iota,\beta) \equiv 2(1+c_i^2)s_{2\beta}F_+ + 4c_i c_{2\beta}F_\times. \tag{4.13b}$$

The Fourier transform can then be computed in the SPA via Eq. (4.5) with $\ell = 2$. We thus obtain

$$\tilde{h}_C(f) = -\left(\frac{5}{384}\right)^{1/2}\pi^{-2/3}\frac{\mathcal{M}^{5/6}}{D_L}Q_C(\iota,\beta) \times [2F(t_0)]^{-7/6}e^{-i(\Psi+\pi/4)}. \tag{4.14}$$

We can solve for the time and phase functions to obtain

$$\phi(F) = \phi_c + 2\pi\int^F \tau' dF' = \phi_c - \frac{1}{32}(2\pi\mathcal{M}F)^{-5/3},$$
$$t(F) = t_c + \int^F \frac{\tau'}{F'}dF' = t_c - \frac{5\mathcal{M}}{256}(2\pi\mathcal{M}F)^{-8/3}, \tag{4.15}$$

where ϕ_c and t_c are the orbital phase and time of coalescence, respectively. Substituting the stationary-phase condition $F(t_0) = f/2$ into these expressions, the phase Ψ becomes

$$\Psi = -2\pi f t_c + \bar{\phi}_c - \frac{3}{128x}, \tag{4.16}$$

where we have defined $x \equiv (\pi\mathcal{M}f)^{5/3}$, and $\bar{\phi}_c$ is the GW phase at coalescence. The argument of the exponential of the Fourier transform is then

$$-i\ln\left[\frac{\tilde{h}_{(\mathrm{circ})}}{|\tilde{h}_{(\mathrm{circ})}|}\right] = 2\pi f t_c - \bar{\phi}_c - \frac{\pi}{4} + \frac{3}{128}(\pi\mathcal{M}f)^{-5/3}, \tag{4.17}$$

and the full Fourier transform becomes

$$\tilde{h}_{(\mathrm{circ})} = -\left(\frac{5}{384}\right)^{1/2}\pi^{-2/3}\frac{\mathcal{M}^{5/6}}{D_L}Q(i,\beta)f^{-7/6} \times \exp\left[i\left(2\pi f t_c - \bar{\phi}_c - \frac{\pi}{4} + \frac{3}{128}(\pi\mathcal{M}f)^{-5/3}\right)\right], \tag{4.18}$$

where $Q = Q_C + iQ_S$. Equation (4.17) is in agreement with well-known results in the literature [55], when we keep in mind that the GW frequency $f = F_{\mathrm{GW}} = 2F$ is usually adopted to write down all results in calculations involving circular binaries.

B. Eccentric case

Let us now focus on eccentric inspirals. Once more, we must consider the response function of the detector, defined by Eq. (4.9), except that now $h_{+,\times}$ correspond to the eccentric waveforms discussed in Sec. III. For eccentric waveforms, the response function becomes

$$h(t) = \mathcal{A}\sum_{\ell=1}^{10}[\Gamma_\ell\cos(\ell l) + \Sigma_\ell\sin(\ell l)], \tag{4.19}$$

where $\mathcal{A}$ is a function of frequency defined in Eq. (3.5), and where we have defined

$$\Gamma_\ell \equiv F_+C_+^{(\ell)} + F_\times C_\times^{(\ell)}, \qquad \Sigma_\ell \equiv F_+S_+^{(\ell)} + F_\times S_\times^{(\ell)}. \tag{4.20}$$

These coefficients are slowly varying functions of time, which can be written as functions of the orbital frequency for some given initial eccentricity e_0. By using the trivial trigonometric identity $\cos(\ell l + \phi) = \cos(\ell l)\times\cos(\phi) - \sin(\ell l)\sin(\phi)$ we can combine terms into a single sum of the form

$$h(t) = \mathcal{A}\sum_{\ell=1}^{10}\alpha_\ell\cos(\ell l + \phi_\ell), \tag{4.21}$$

where

$$\alpha_\ell = \mathrm{sgn}(\Gamma_\ell)\sqrt{\Gamma_\ell^2 + \Sigma_\ell^2}, \tag{4.22a}$$

$$\phi_\ell = \tan^{-1}\left(-\frac{\Sigma_\ell}{\Gamma_\ell}\right). \tag{4.22b}$$

We shall not present the coefficients α_ℓ and ϕ_ℓ here, but they can be straightforwardly calculated using results from the previous section.

The Fourier transform in the SPA then becomes

$$\tilde{h} = -\left(\frac{5}{384}\right)^{1/2}\pi^{-2/3}\frac{\mathcal{M}^{5/6}}{D_L}[2F(t_0)]^{-7/6} \times \frac{(1-e^2)^{7/4}}{(1+\frac{73}{24}e^2+\frac{37}{96}e^4)^{1/2}} \times \sum_{\ell=1}^{10}\alpha_\ell\sqrt{\frac{2}{\ell}}e^{-i\phi_\ell[F(t_0)]}e^{-i(\Psi+\pi/4)}, \tag{4.23}$$

where we have used the fact that for eccentric orbits the orbital phase evolution is given by [9]

$$\frac{dF}{dt} = \frac{da}{dt}\frac{dF}{da} = \frac{48}{5\pi\mathcal{M}^2}(2\pi\mathcal{M}F)^{11/3}\frac{(1+\frac{73}{24}e^2+\frac{37}{96}e^4)}{(1-e^2)^{7/2}}. \tag{4.24}$$

The frequency that appears in Eq. (4.23) can be thought of as an *instantaneous mean orbital frequency*. Such a quantity is "instantaneous" in the sense that it evolves on a radiation-reaction time scale. The factor of $1/\sqrt{\ell}$ comes about due to the factor of $(d^2\phi/dt^2)^{-1/2}$ in Eq. (4.5). Also note that now $\phi(t_0) = \ell l(t_0)$ and the factor of ϕ_ℓ cannot be pulled out of the sum because it depends on ℓ. One can check that in the limit $e_0 \to 0$, $\alpha_2 e^{-i\phi_2} \to Q$ and we recover the circular limit.

The phase Ψ must be evaluated at the stationary point t_0, which is here defined implicitly via $\ell\dot{l}(t_0) = 2\pi f$ or simply $F(t_0) = f/\ell$, as already discussed. The phase Ψ is then essentially Eq. (4.8), which requires knowledge of the characteristic time scale τ. Unlike the circular case, for eccentric inspirals the integral over τ can only be done approximately, since

$$\tau = \frac{5\mathcal{M}}{96}(2\pi\mathcal{M}F)^{-8/3}\frac{(1-e^2)^{7/2}}{1+\frac{73}{24}e^2+\frac{37}{96}e^4}, \tag{4.25}$$

and e is a slowly varying function of F that cannot be inverted in closed form. We can achieve this inversion asymptotically for small eccentricities, by first expanding Eq. (4.25) in $e \ll 1$

$$\tau \sim \frac{5\mathcal{M}}{96}(2\pi\mathcal{M}F)^{-8/3}\left[1-\frac{157}{24}e^2+\frac{13\,759}{576}e^4 - \frac{999\,793}{13\,824}e^6+\frac{70\,021\,111}{331\,776}e^8+\mathcal{O}(e^{10})\right]. \tag{4.26}$$

Since the eccentricity as a function of frequency is given by Eq. (3.11), the characteristic time becomes

$$\tau \sim \frac{5\mathcal{M}}{96}(2\pi\mathcal{M}F)^{-8/3}\left\{1-\frac{157}{24}e_0^2\chi^{-19/9}+e_0^4\left[\frac{1\,044\,553}{21\,888}\chi^{-38/9}-\frac{521\,711}{21\,888}\chi^{-19/9}\right] + e_0^6\left[\frac{3\,471\,049\,619}{9\,980\,928}\chi^{-38/9}-\frac{265\,296\,245}{4\,990\,464}\chi^{-19/9}-\frac{135\,641\,025}{369\,664}\chi^{-19/3}\right] + e_0^8\left[-\frac{450\,735\,126\,075}{112\,377\,856}\chi^{-19/3}+\frac{25\,654\,857\,812\,777}{18\,205\,212\,672}\chi^{-38/9}+\frac{158\,823\,466\,804\,555}{54\,615\,638\,016}\chi^{-76/9} - \frac{1\,301\,043\,440\,515}{13\,653\,909\,504}\chi^{-19/9}\right]+\mathcal{O}(e_0^{10})\right\}, \tag{4.27}$$

where as usual $\chi \equiv F/F_0$. This is a generalization of Eq. (A8) of Ref. [37] to higher powers of eccentricity.

We can now compute the new phase [Eq. (4.8)] by integrating the characteristic time. Using the stationary-phase condition $F(t_0) = f/\ell$, we obtain

$$\Psi_\ell = \ell\phi_c - 2\pi f t_c - \frac{3}{128x}\left(\frac{\ell}{2}\right)^{8/3}\left[1-\frac{2355}{1462}e_0^2\chi^{-19/9}+e_0^4\left(\frac{5\,222\,765}{998\,944}\chi^{-38/9}-\frac{2\,608\,555}{444\,448}\chi^{-19/9}\right) + e_0^6\left(-\frac{75\,356\,125}{3\,326\,976}\chi^{-19/3}-\frac{1\,326\,481\,225}{101\,334\,144}\chi^{-19/9}+\frac{17\,355\,248\,095}{455\,518\,464}\chi^{-38/9}\right) + e_0^8\left(-\frac{250\,408\,403\,375}{1\,011\,400\,704}\chi^{-19/3}+\frac{4\,537\,813\,337\,273}{39\,444\,627\,456}\chi^{-76/9}-\frac{6\,505\,217\,202\,575}{277\,250\,217\,984}\chi^{-19/9} + \frac{128\,274\,289\,063\,885}{830\,865\,678\,336}\chi^{-38/9}\right)+\mathcal{O}(e_0^{10})\right], \tag{4.28}$$

where we recall that $x \equiv (\pi\mathcal{M}f)^{5/3}$, and Ψ has now become a function of ℓ. We have checked that the first few terms in the phase of Eq. (4.28) agree with the phase computed in Eq. (A10) of [37]. Notice that when we apply the stationary-phase condition to $e(F)$ we must also rescale $F_0 \to f_0/\ell$, so that $e(f_0) = e_0$. Otherwise, the eccentricity function would not be properly normalized.

Combining all pieces together we obtain the Fourier transform in the SPA, namely,

$$\tilde{h} = \tilde{\mathcal{A}} f^{-7/6} \sum_{\ell=1}^{10} \xi_\ell \left(\frac{\ell}{2}\right)^{2/3} e^{-i(\pi/4+\Psi_\ell)}, \tag{4.29}$$

where we have defined

$$\tilde{\mathcal{A}} = -\left(\frac{5}{384}\right)^{1/2} \pi^{-2/3} \frac{\mathcal{M}^{5/6}}{D_L}, \tag{4.30}$$

$$\xi_\ell = \frac{(1-e^2)^{7/4}}{(1+\frac{73}{24}e^2+\frac{37}{96}e^4)^{1/2}} \alpha_\ell e^{-i\phi_\ell(f/k)}. \tag{4.31}$$

This is the Fourier transform of the waveform for eccentric inspirals in the SPA. Note that we have kept up to ten harmonics, which corresponds to a consistent expansion in the eccentricity to $\mathcal{O}(e^8)$ both in the amplitude and in the phase. We already saw in Sec. II that this is enough to model the Bessel function to high accuracy even for relatively high eccentricities.

The Fourier transform presented here depends on the coefficients ξ_ℓ that need to be *reexpanded* in the limit $e_0 \ll 1$. These coefficients can be obtained from Eq. (4.31), using the definition of $e(F)$ in Eq. (3.11), α_ℓ in Eq. (4.22a), ϕ_ℓ in Eq. (4.22b) and Γ_ℓ and Σ_ℓ in Eq. (4.20), where $C_{+,\times}$ and $S_{+,\times}$ are given in Appendix B. The resulting expression must then be reexpanded in the limit $e_0 \ll 1$ to $\mathcal{O}(e_0^8)$. We shall not present these expressions here in full generality, since they are lengthy and complicated. Instead we present partial results for ξ_k as a function of $e(F)$ in Appendix C for an optimally oriented binary ($\iota = \beta = 0$). In the next section, we shall employ these expressions in combination with Eq. (3.11), and reexpand them in $e_0 \ll 1$ to eighth order to compute the SNR.

V. SNR CALCULATION

In this section we compute the SNR using the Fourier transform of the waveform in the SPA [Eq. (4.29)]. The SNR is defined via

$$\rho^2 \equiv 4\Re \int_{f_{\rm low}}^{f_{\rm high}} \frac{\tilde{h}\tilde{h}^\star}{S_n(f)} df, \tag{5.1}$$

where $S_n(f)$ is the one-sided noise power spectral density and the star superscript stands for complex conjugation. The noise curves of the AdvLIGO, ET and LISA detectors are taken from Refs. [65–67], respectively; for LISA, in particular, we adopt the simple ''angle-averaged'' model discussed in [65].

A. Limits of integration

The upper frequency of integration $f_{\rm high}$ is either the frequency at which the motion transitions from inspiral to plunge or the maximum frequency at which the detector noise is under control. Since the noise power spectral densities for LIGO and ET increase steeply at high frequency, we will choose

$$f_{\rm high}^{\rm LISA} = \min[2F_{\rm ISCO}, 1\ {\rm Hz}], \tag{5.2}$$

$$f_{\rm high}^{\rm LIGO} = f_{\rm high}^{\rm ET} = 2F_{\rm ISCO}. \tag{5.3}$$

In the previous equations, as customary in the GW literature, we (somewhat arbitrarily) pick the ISCO frequency to be $F_{\rm ISCO} \equiv 6^{-3/2}(2\pi M)^{-1}$, in analogy with the orbital frequency of a test particle at the ISCO of the Schwarzschild spacetime. In Appendix D we discuss possible eccentricity-induced modifications to this conventional ISCO frequency, concluding that such modifications should not introduce significant corrections to our SNR calculations.

The lower limit of integration $f_{\rm low}$ is determined by a seismic (or acceleration) noise cutoff:

$$f_{\rm low}^{\rm LIGO} = f_s^{\rm LIGO} = 20\ {\rm Hz}, \qquad f_{\rm low}^{\rm ET} = f_s^{\rm ET}, \qquad f_{\rm low}^{\rm LISA} = f_{\rm acc} = 10^{-4}\ {\rm Hz}, \tag{5.4}$$

where we shall investigate the ET SNR with $f_s^{\rm ET} = 1$ Hz or $f_s^{\rm ET} = 10$ Hz. The quantity $f_{\rm acc}$ corresponds to the minimum frequency at which acceleration noise is under control in LISA.

Different harmonic components will generically sample different frequency ranges if we terminate all integrations when the dominant quadrupole GW frequency equals the ISCO frequency. To ensure that higher harmonics do not exceed the region of validity, following [43], we shall truncate the waveforms with unit step functions $\Theta(x)$ [$\Theta(x) = 1$ if $x \geq 0$ and zero otherwise]):

$$\tilde{h}_{\rm LIGO/ET} = \tilde{\mathcal{A}} f^{-7/6} \sum_{\ell=1}^{10} \left(\frac{\ell}{2}\right)^{2/3} \xi_\ell e^{-i\Psi_\ell} \Theta(\ell f_{\rm high}^{\rm LIGO/ET} - 2f), \tag{5.5}$$

where we have removed the factor of $\pi/4$ in the phase, since it cancels out in SNR calculations. The step function guarantees that higher harmonics are truncated at the correct upper frequency cutoff.

LISA sources can spend several years in the LISA band, an issue that must be accounted for, since the detector will not take data for more than a few years. Following [43,65], we shall multiply the waveform by an additional step function:

$$\tilde{h}_{\rm LISA} = \frac{\sqrt{3}}{2} \tilde{\mathcal{A}} f^{-7/6} \sum_{\ell=1}^{10} \left(\frac{\ell}{2}\right)^{2/3} \xi_\ell e^{-i\Psi_\ell} \times \Theta(\ell f_{\rm high}^{\rm LISA} - 2f)\Theta(2f - \ell f_{\rm yr}^{\rm LISA}), \tag{5.6}$$

where $f_{\rm yr}$ is the GW frequency of the fundamental harmonic at a time T before the system reaches the ISCO (see Appendix E for a discussion of how to calculate this

quantity for eccentric inspirals). We shall here choose T to be equal to 1 yr (hence assuming, somewhat optimistically, that we can observe the whole last year of inspiral). This step-function cutoff guarantees that all harmonics are integrated for no more than 1 yr, which is the higher-harmonic generalization of the criterion used in [65]. Note also that we have multiplied the LISA waveform amplitude by a geometrical correction factor of $\sqrt{3}/2$ (see [65,68] for details).

With these considerations in mind, the SNR is given by

$$\rho_A^2 = 4\Re \int_{f_{\rm low}^A}^{\ell_{\rm max} f_{\rm high}^A} \frac{\tilde{h}_A \tilde{h}_A^\star}{S_n^A} df, \tag{5.7}$$

where A stands for any of LIGO, ET or LISA. Caution should be exercised in comparing results between different detectors. Even for astrophysical systems with the same masses, different detectors have different low-frequency cutoffs, and the initial eccentricity e_0 is defined as the value of e at that frequency. For example, a $100M_\odot$ system with $e_0 = 0.3$ does not correspond to the same astrophysical system when we discuss AdvLIGO, whose seismic cutoff is 20 Hz, and when we discuss ET, whose seismic cutoff is 10 or 1 Hz.

B. Results

Figure 6 plots the SNR for an equal-mass system as a function of the total binary mass expressed in solar mass units. This SNR is computed at the optimal binary orientation ($\iota = \beta = \theta_S = \phi_s = \psi_S = 0$). As discussed earlier, for each detector the initial eccentricity is computed at some (somewhat conventional) lowest cutoff frequency, which is different for each detector. We recall that for AdvLIGO and ET this lower cutoff corresponds to the seismic noise "wall" (20 and either 1 or 10 Hz), while for LISA we (conservatively) adopt a lower cutoff at 10^{-4} Hz.

As a generic trend, the mass reach increases by as much as a factor of 5 for the largest initial eccentricities explored here. For systems with $e_0 = 0.4$ AdvLIGO could observe binaries with total mass up to $10^3 M_\odot$, ET could see sys-

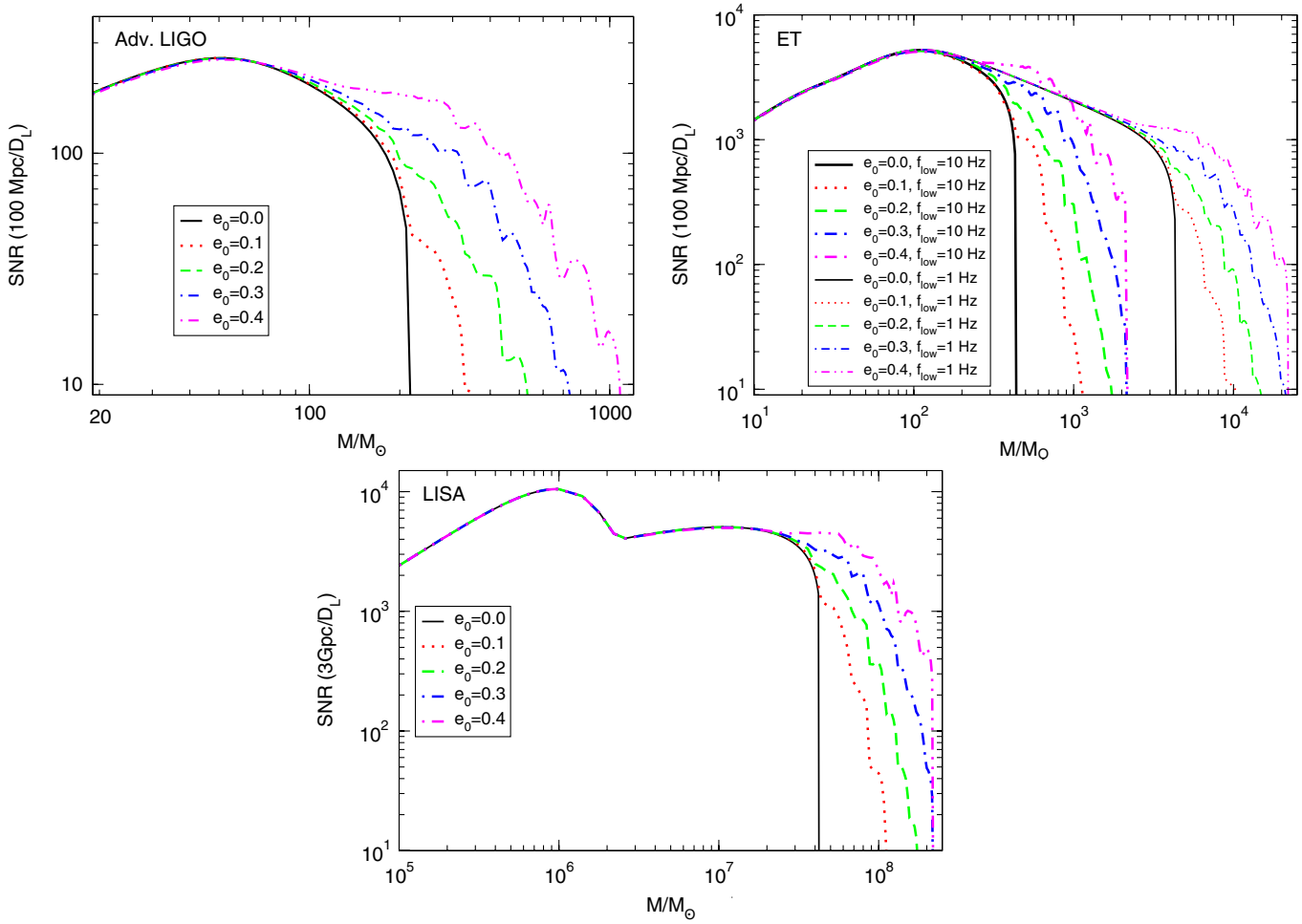

FIG. 6 (color online). SNR for an equal-mass binary at optimal orientation as a function of total mass in solar mass units for different initial eccentricities. The top figures correspond to the AdvLIGO (left) and ET (right) detectors, while results for the LISA detector are shown in the bottom panel.

tems up to $2 \times 10^3 M_\odot$ or $2 \times 10^4 M_\odot$ (for a 10 or a 1 Hz low-frequency cutoff, respectively), and LISA could see binaries up to $2 \times 10^8 M_\odot$. This is to be compared to circular inspiral mass reaches of approximately $200 M_\odot$ for AdvLIGO, $400 M_\odot$ or $4 \times 10^3 M_\odot$ for ET (for a 10 or a 1 Hz low-frequency cutoff) and $4 \times 10^7 M_\odot$ for LISA.

Another feature of this figure is that for low-mass systems, the circular SNR curve seems to overlap that of eccentric binaries. One can understand this by noting that low-mass systems merge in the high-frequency band of the detector, since the merger frequency is inversely proportional to the total mass. In such cases, the binary circularizes before merger. Suppose that the binary's eccentricity reduces to $e_0 \leq 10^{-2}$ at some "circularization frequency" F_c. One can then compare the number of cycles the binary spends in $\{f_{\rm low}, F_c\}$ relative to the number of cycles spent in $\{F_c, F_{\rm high}\}$, to find that the latter is overwhelmingly large for low-mass systems. Such a fact does not imply that circular waveforms are sufficient for detection or parameter estimation from eccentric inspirals of low mass. The SNRs shown here are "optimal," and thus, a much more careful fitting-factor study is necessary to determine whether circular templates suffice to extract eccentric binary signals.

For high masses the SNR presents a somewhat oscillatory behavior. These oscillations seem to scale with the eccentricity, becoming worse for systems with $e_0 = 0.4$. Oscillations are expected, since different harmonics could interfere in the SNR integrand and since the step-function truncation of the waveforms will introduce oscillations at overtones of the truncation frequencies. We discuss these issues in more detail in the next subsection.

C. Accuracy of the approximation

An important issue concerns the accuracy of our post-circular approximation. Our approximation is essentially an expansion for $e_0 \ll 1$, so it should break down as we increase the initial eccentricity. On the other hand, if the condition $e_0 \ll 1$ is verified, a relatively small number of harmonics should model the waveform accurately enough that we would not lose much in terms of SNR.

In order to explore this issue, in Fig. 7 we plot the absolute value $\delta\rho(\ell_{\rm max}, 10) \equiv |\rho(\ell_{\rm max}) - \rho(10)|$, where $\rho(\ell_{\rm max})$ is the SNR computed by keeping $\ell_{\rm max}$ terms in the harmonic sum of Eq. (4.29). In the top two panels we consider systems with moderate initial eccentricity ($e_0 = 0.01$ and $e_0 = 0.1$), which are probably most relevant for several classes of astrophysical GW sources. When $e_0 = 0.01$, the deviation in SNR relative to the highest-order terms we computed ($\ell_{\rm max} = 10$) is at most of $\mathcal{O}(1)$ or of $\mathcal{O}(10^{-1})$ when one uses $\ell_{\rm max} = 2$ and $\ell_{\rm max} = 3$, respectively. On the other hand, for the $e_0 = 0.1$ case, a comparable accuracy in SNR requires $\ell_{\rm max} \geq 4$ and $\ell_{\rm max} \geq 5$, respectively. It should not be surprising that a smaller number of harmonics is required for systems with low eccentricity. Our analysis suggests that summing up to $\ell_{\rm max} \simeq 4$ should be enough for systems with $e_0 \leq 0.1$, while for systems with $0.1 < e_0 \leq 0.3$ one needs $\ell_{\rm max} \geq 8$.

More interesting features emerge for larger values of e_0 (bottom panels in Fig. 7), which we list below:

(1) Different harmonics play a critical role in the SNR at different mass ranges. When $e_0 = 0.3$ the SNR difference peaks at approximately $(200, 400, 500, 600) M_\odot$ for $\ell_{\rm max} = (2, 3, 4, 5)$; for lower and larger masses, a smaller number of harmonics is necessary.

(2) The number of harmonics necessary to cover the entire mass range is a function of the initial eccentricity e_0. When $e_0 = 0.3$, for example, harmonics with $\ell > 7$ are not needed, because $\delta\rho(6, 10) < 7$ in the entire mass range. On the other hand, for the $e_0 = 0.4$ case, one really needs at least $\ell_{\rm max} = 9$ to obtain errors $\delta\rho(9, 10) < 10$ in the whole mass range, while for $e_0 = 0.5$ the approximation seems to break down, unless more harmonics are included.

(3) The oscillations visible in the plots are not necessarily an artifact of the post-circular approximation. Indeed, these oscillations are also present in the small-eccentricity curves $[e_0 = (0.1, 0.2, 0.3)]$ of Fig. 6 and in the top panel $[e_0 = (0.01, 0.1)]$ of Fig. 7. If these oscillations were an artifact of the post-circular approximation, they would vanish in the small-eccentricity limit, but instead, although they decrease in magnitude, they are still present.

The fact that different harmonics peak at different masses can be understood by observing that two competing effects control the SNR difference: the eccentricity decay and the frequency band over which we perform the integration. For small masses, one is integrating over a larger frequency band, and the binary rapidly circularizes before merging. Less harmonics are needed in the limit of very small mass, since the binary is essentially circular before reaching the most sensitive region of the detector. On the other hand, for really high masses one is integrating for short times and essentially capturing only the behavior near the ISCO. In such cases, the SNR difference is converging to zero, because the SNRs themselves are essentially vanishing (i.e. the range of integration asymptotes to zero).

The oscillatory features can be understood by studying the analytic structure of the waveforms used to compute the SNRs. For small eccentricities, the oscillations are probably due to interference between the different harmonics and to the use of step functions to truncate the SNR at different harmonics. The waveform contains a sum of ten different oscillatory functions, and when this sum is multiplied by its complex conjugate, one naturally obtains interference of the type $\exp[i(\ell - \ell')t]$. Moreover, the step-function truncation of the SNR also forces oscillations at overtones of the ISCO frequency. For example, Figs. 6 and 7 show oscillations at $\ell F_{\rm ISCO}$, with $\ell = \{1, 10\}$. This is

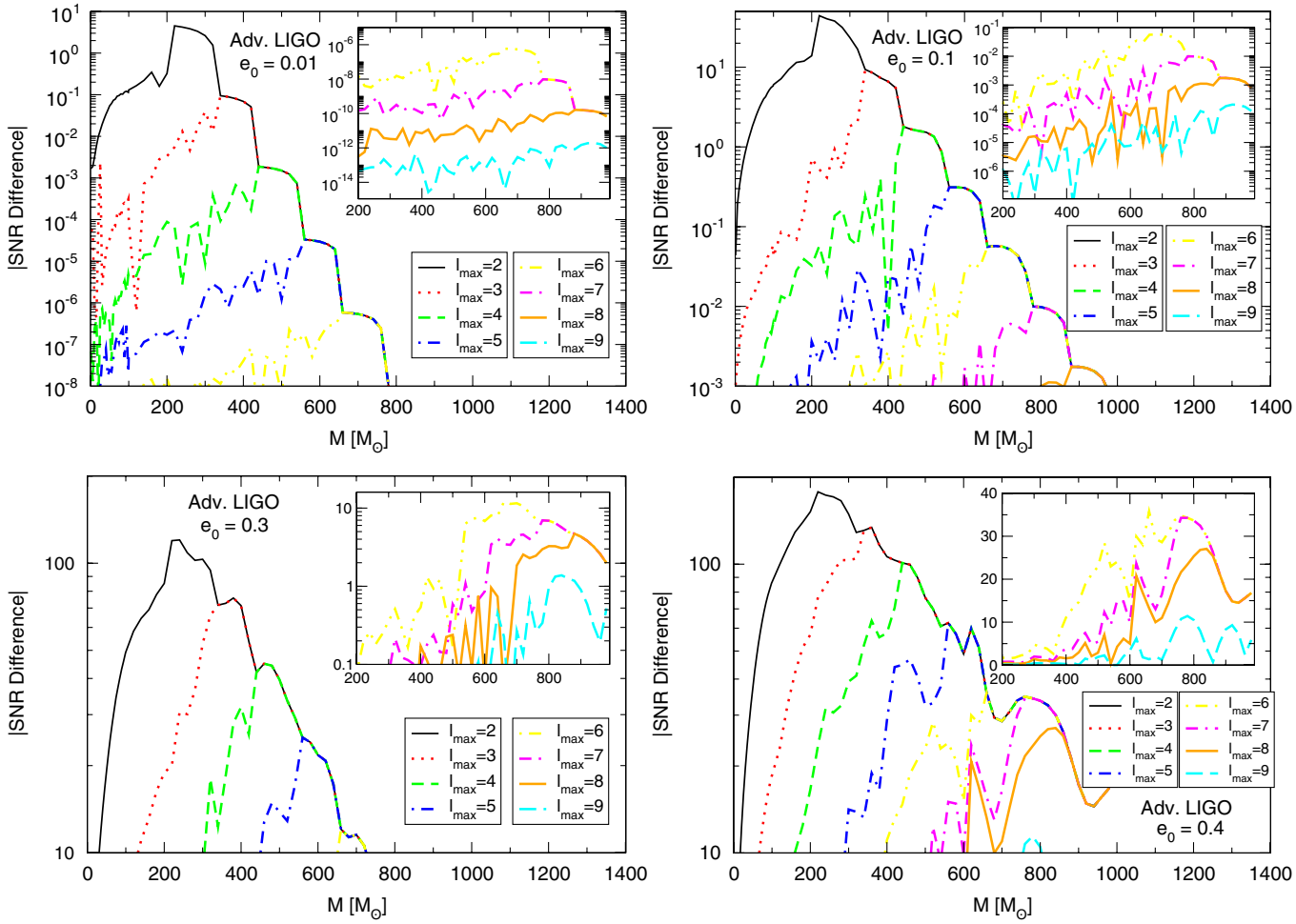

FIG. 7 (color online). Absolute value of the difference in SNR computed up to $\ell_{\max} = (2, 3, 4, 5, 6, 7, 8, 9)$ and up to $\ell_{\max} = 10$. We use the AdvLIGO noise curve and an initial eccentricity of $e_0 = 0.01$, $e_0 = 0.1$, $e_0 = 0.3$ and $e_0 = 0.4$ (top to bottom). The insets zoom on the y axis in the region between 200 and 800 solar masses.

because the leading harmonic has a mass reach corresponding to twice the ISCO frequency, whereas the ℓth harmonic has a mass reach corresponding to ℓ times the ISCO frequency. Since we use a step-function cutoff for every harmonic [see e.g. Eq. (5.5)], the resulting SNR will show the "bumps" seen in Fig. 7. Of course, although there are analytic reasons that explain the presence of these oscillations, one cannot formally exclude the possibility that (for large e_0) some of these oscillations are induced by inaccuracies in the post-circular approximation.

D. Angular dependence

In all SNR plots, we have so far assumed that binaries are optimally oriented. This is a very special configuration, and it is important to investigate the variations in SNR for nonoptimally oriented binaries. Figure 8 shows histograms of the SNR distribution under the hypothesis of a uniform distribution of the angles involved: the angles (ι, β) describing the orientation of the source and the three angles $(\theta_S, \phi_S, \psi_S)$ appearing in the antenna pattern functions [65]. We binned the data of the 1000 random realizations in bins of 50. The histograms are representative of the number of realizations in each bin. Since they are normalized, the numbers on the vertical axis do not correspond to the actual number of realizations in each bin. The comparison of distributions corresponding to various eccentricities makes sense only if the histograms are normalized. In the two panels of Fig. 8 we plot the AdvLIGO SNR distribution for two representative binaries with total mass $100M_\odot$ (left panel) and $300M_\odot$ (right panel). The SNR of the $100M_\odot$ system is dominated mostly by the leading harmonic, whereas the $300M_\odot$ system has a significant contribution from higher harmonics (see the top panel of Fig. 6). In each panel we show three histograms, corresponding to initial eccentricities $e_0 = 0.1$ (dotted black), 0.2 (dashed blue) and 0.4 (solid red).

The effect of eccentricity is to shift the SNR distribution to higher masses. For the $100M_\odot$ system, although the SNR

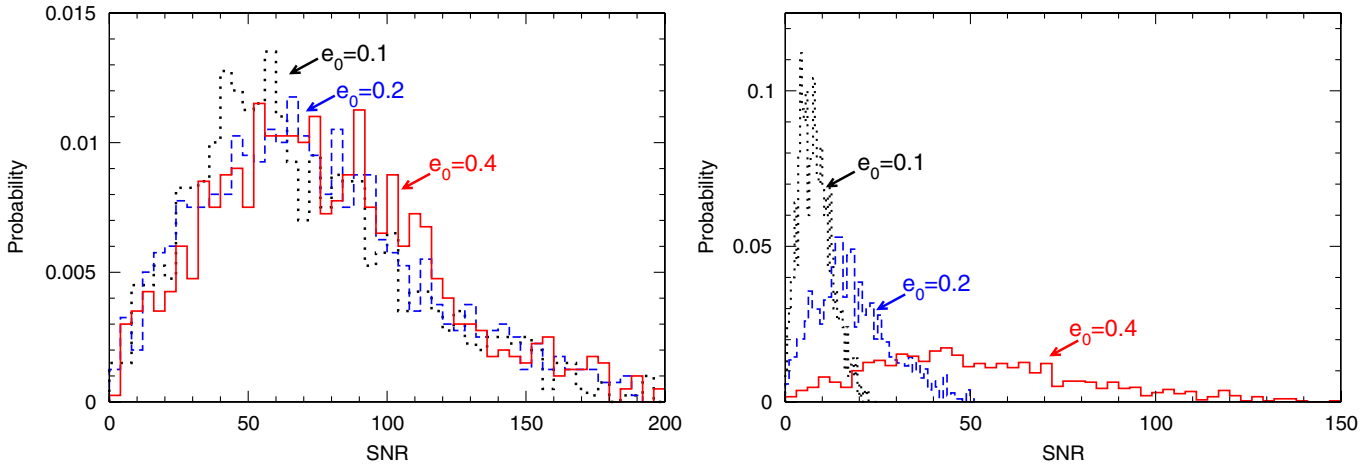

FIG. 8 (color online). Histograms of the AdvLIGO SNR (see text) for a set of random observer orientations. The left (right) panel corresponds to a $M = 100M_\odot$ ($M = 300M_\odot$) system. Systems with initial eccentricity $e_0 = (0.1, 0.2, 0.4)$ are shown in dotted black, dashed blue and solid red, respectively.

distribution visibly shifts to the right, the effect is rather mild for the initial eccentricities considered in the plot. In this case, the distributions look more or less similar, except for a longer tail at large SNRs for large initial eccentricities. For the $300M_\odot$ system, the shift in the distribution is much more pronounced. While the distribution is narrowly peaked at low eccentricities, it becomes much wider for larger eccentricities. This widening of the distribution might be because, for large eccentricities, the waveforms are more sensitive to terms proportional to $c_i = \cos\iota$ (see the expressions of $C_+^{(n)}$ and $S_+^{(n)}$ in Appendix B). These amplitude corrections, being proportional to the eccentricity, are suppressed for small values of e_0.

The SNR histograms show that, although the SNR values for any particular observation may deviate considerably from the optimal values we have quoted, the general trends in the SNR induced by eccentricity (mass reach increase, accessible volume increase) will not be modified. That is, regardless of the location of the source in the sky, eccentricity has the net effect of increasing the SNR or mass reach of any given signal.

VI. PN CORRECTIONS

Although this paper has only considered Newtonian waveforms to exemplify the post-circular construction of the SPA Fourier transform of eccentric waveforms, it is instructive to discuss how to extend these results to higher PN order. In this section we shall mainly follow the conventions of Gopakumar and Iyer [50], where a "2PN term" is one of $\mathcal{O}(\dot{r}/c)^4$ smaller than the leading-order term; i.e. we employ a *relative* order counting scheme.

When eccentric orbits are studied beyond 1PN order, one discovers that the Keplerian parametrization must be corrected. In particular, Eqs. (2.1) and (2.3) are enhanced by new $\mathcal{O}(\dot{r}/c)^2$ corrections, while Eq. (2.2) is enhanced by corrections of $\mathcal{O}(\dot{r}/c)^4$. Moreover, if we want to keep a Keplerian-inspired parametrization we must introduce *three* distinct eccentricity parameters: e_r measures radial oscillations, e_ϕ measures azimuthal oscillations and e_t measures the frequency eccentricity. These eccentricity parameters can be written as functions of e_t in a PN expansion, but this choice is somewhat arbitrary (see e.g. [69] for comparisons of the different definitions with numerical relativity simulations of eccentric mergers).

The waveforms then acquire two sets of modifications: amplitude and phase corrections. The amplitude corrections, as expected, take the form

$$h_{+,\times} \approx \frac{m\eta}{R}\zeta^{2/3}[H^{(0)}_{+,\times} + \zeta^{1/2}H^{(1/2)}_{+,\times} + \zeta H^{(1)}_{+,\times} + \cdots], \tag{6.1}$$

where $\zeta \equiv mN$ is a natural PN expansion parameter of $\mathcal{O}(\dot{r}/c)^2$, $\eta = \mu m$ is the symmetric mass ratio and $H^{(n)}_{+,\times}$ are products of functions of the eccentricities and harmonic trigonometric functions. The phase corrections can be split into

$$\phi - \phi_0 = \lambda(l) + W(l), \tag{6.2}$$

where $\lambda(l)$ is a $2\pi K$-periodic function of the mean anomaly, while $W(l)$ is periodic in l, and thus, 2π-periodic. The quantity K measures the advance of the periastron per orbital revolution [19], while the effect of $W(l)$ is to modulate the amplitude via nutation.

The leading-order correction to the phasing of GWs is due to pericenter precession. This effect is embodied in the function $\lambda(l)$, which can be written as

$$\lambda(l) = Kl = [1 + k_p(e_t)]l, \tag{6.3}$$

where we have defined $K = 1 + k_p(e_t)$. To this order, the

mean anomaly continues to be given by Eq. (2.2) with $e \to e_t$, while the precessional correction $k_p(e_t)$ is given by

$$k_p(e_t) = \frac{3\zeta^{2/3}}{1-e_t^2} + \mathcal{O}(\dot{r}/c)^4. \tag{6.4}$$

Since N appears here as a 1PN order correction, we can take its Newtonian value in this equation, namely, $N = 2\pi f$, such that $\zeta = 2\pi MF$. Thus, the precessional correction becomes

$$k_p(e_t) = \frac{3(2\pi MF)^{2/3}}{1-e_t^2} + \mathcal{O}(\dot{r}/c)^4. \tag{6.5}$$

We can expand this function for small eccentricities $e_t \ll 1$ to find

$$\lambda(l) \sim l[1 + 3(2\pi MF)^{2/3}(1 + e_t^2 + e_t^4 + e_t^6 + e_t^8)]. \tag{6.6}$$

The second correction to the phase is given by the nutation function W, defined by

$$W = (\upsilon - u + e_t \sin u)[1 + k_p(e_t)] + \mathcal{O}(\dot{r}/c)^4, \tag{6.7}$$

where the true anomaly is given by

$$\upsilon = 2\tan^{-1}\left[\left(\frac{1+e_\phi}{1-e_\phi}\right)^{1/2}\tan\left(\frac{u}{2}\right)\right]. \tag{6.8}$$

Note that the true anomaly depends on e_ϕ and not e_t, but these quantities are related via

$$e_\phi = e_t[1 + \zeta^{2/3}(4-\eta) + \mathcal{O}(\dot{r}/c)^4]. \tag{6.9}$$

In Sec. II we already discussed how to solve for u as a function of l in terms of a series of Bessel functions. In particular, one can show that

$$u = l + \sum_{s=1}^{\infty}\left(\frac{2}{s}\right)J_s(se)\sin(sl). \tag{6.10}$$

Equations (6.9) and (6.10) can be substituted in Eq. (6.8) to find υ as a function of l. Then Eq. (6.7) yields W as a function of l. Expanding in $e_t \ll 1$ one finds

$$\begin{aligned} W(l) \sim\ & e_t[-(-10+\eta)\zeta^{2/3} + 2]\sin(l) \\ & + e_t^2[-1/2(4\eta - 31)\zeta^{2/3} + 5/2]\cos(l)\sin(l) \\ & + e_t^3[(-1/6(-186 + 27\eta)\zeta^{2/3} + 13/3) \\ & \times \cos^2(l) - 1/6(12 - 6\eta)\zeta^{2/3} - 4/3]\sin(l) + \cdots. \end{aligned} \tag{6.11}$$

This function, however, is part of the phase, so it enters the waveform as the argument of trigonometric functions. Note that $W(l)$ is linear in e_t, and thus, when the $\cos(\phi)$ or $\sin(\phi)$ are expanded in $e_t \ll 1$, $W(l)$ introduces higher harmonics into the waveforms.

We see then that to 1PN order, it suffices to consider the pericenter precession correction through λ. The corrections produced by $W(l)$ are automatically accounted for in the Bessel expansion. In essence, this is because Eqs. (2.1) and (2.2) are not modified to this order. The 1PN-corrected waveforms are then (schematically)

$$\begin{aligned} h(t) = \mathcal{A}\sum_{\ell=1}^{10}\alpha_\ell \cos\{\ell l[1 + 3(2\pi MF)^{2/3} \\ \times (1 + t_2 e_t^2 + t_4 e_t^4 + t_6 e_t^6)] + \phi_\ell\}, \end{aligned} \tag{6.12}$$

where the t_k's are constants. If we were to consider 2PN corrections to the waveforms, then the formalism outlined here would have to be extended and $W(l)$ would contribute by introducing new corrections not accounted for in the Bessel expansion.

The structure of the 1PN time-domain waveform in Eq. (6.12) is different from that obtained in Refs. [38,39], in that the above equation does not lead to periastron-precession sidebands in the GW spectrum. In Refs. [38,39] such sidebands arise due to the assumption that periastron precession leads to a constant $\dot{\gamma} \propto k_p$. This assumption breaks down on long time scales as periastron precession is not constant, an effect one can justly treat as a 1PN contribution. As a result, one loses the artificial sideband structure in the GW spectrum. The implications of this effect will be assessed in future work.

PN corrections modify the Fourier transform of the waveform in the SPA. The phase $\bar{\Psi}_\ell$ is modified by a factor of $(1 + k_p)$, and we now obtain

$$\Psi_\ell(F) = k\lambda[t(f/\ell)] - 2\pi f t(f/\ell), \tag{6.13}$$

where

$$\begin{aligned} \lambda[t(f/\ell)] &= \ell\phi_c + \ell\int^{f/\ell}\frac{\dot{\lambda}'}{\dot{F}}dF', \\ t(f/\ell) &= t_c + \int^{f/\ell}\frac{dF'}{\dot{F}'}. \end{aligned} \tag{6.14}$$

The $\dot{\lambda}$ term contains the $(1 + k_p)$ dependence that we referred to via Eq. (6.3). All the machinery developed in the previous section then carries through, with the proper enhancement of the Newtonian waveform to higher PN order. The net effect of higher PN corrections in the Fourier transform is to introduce an infinite set of harmonics and PN corrections to the lower-order (Newtonian) harmonics considered earlier.

While considering higher PN order effects, one can also work with the PN parameter $(M\omega)^{2/3}$, where ω is the orbital frequency. As pointed out in Ref. [20], this parametrization helps to more easily recover the circular limits of various elliptic-orbit expressions. Furthermore, in comparing numerical relativity results to PN expansions, Ref. [70]

found that waveforms parametrized in terms of $(M\omega)^{2/3}$ are in better agreement with numerical waveforms. This deserves more careful study in the future.

VII. CONCLUSIONS

We have proposed a new scheme, the post-circular approximation, to construct ready-to-use, analytic Fourier-domain gravitational waveforms produced by eccentric binary inspirals. The scheme consists of expanding all quantities in a power series about zero initial eccentricity. We find that the first 10 terms in the Bessel solution to the Kepler problem suffice to reproduce the eccentricity evolution to better than 0.1% for eccentricities $e < 0.4$. The resulting waveforms are then rewritten in terms of ten physical parameters (the reduced mass η, the initial eccentricity e_0 and frequency F_0, the total mass M, the luminosity distance D_L, four angles ι, β, θ, and ϕ describing the relative orientation of the source and detector, and a polarization angle ψ) and the orbital frequency, which can be thought of as a function of time.

This scheme allows us to analytically construct the Fourier transform of the response function through the SPA, where one assumes that the radiation-reaction time scale is much larger than the orbital time scale. The resulting Fourier-domain waveforms contain eccentricity-induced, higher-harmonic amplitude and phase corrections. By computing the SNR as a function of total mass and eccentricity we find that the amplitude corrections increase the mass reach of the detectors by a factor $\simeq 5$ for moderately eccentric systems, which in turn implies that the source volume accessible to the detectors would be increased by almost 2 orders of magnitude.

The results presented here cannot be used directly in realistic data analysis pipelines because PN corrections to the amplitude and phase have not been included. Instead, the present paper was concerned with proposing a method to construct ready-to-use, analytic expressions for the Fourier transform of the response function, which was exemplified through Newtonian-accurate expressions. Future research should include such PN corrections.

Another interesting research direction is the study of the effect of eccentricity in parameter estimation. Eccentricity adds more complexity and information to the waveforms that could break parameter degeneracies, thus possibly leading to better accuracy in parameter estimation. On the other hand, the inclusion of eccentricity-induced corrections to the GW phase could mimic certain high-order PN phase corrections, which would then create new degeneracies. A more detailed parameter estimation study is needed to assess whether GW measurements will benefit or not from the inclusion of eccentricity.

While finalizing the draft we learned that two different groups are investigating frequency-domain gravitational waveforms for eccentric binaries [71,72]. It would be interesting to compare their approach with ours and with the time-domain waveforms of [29].

ACKNOWLEDGMENTS

We thank Eric Poisson, Sai Iyer, David Spergel and Frans Pretorius for very useful discussions. K. G. A. and C. M. W. were supported in part by the National Science Foundation, Grant No. PHY 06-52448, the National Aeronautics and Space Administration, Grant No. NNG-06GI60G, and the Centre National de la Recherche Scientifique, Programme Internationale de la Coopération Scientifique (CNRS-PICS), Grant No. 4396. N. Y. acknowledges support from NSF Grant No. PHY-0745779. E. B. acknowledges support from NSF Grant No. PHY-0900735.

APPENDIX A: LISA ECCENTRIC BINARIES

In this appendix we briefly review some literature on scenarios leading to noneccentric binary inspirals in the LISA band. We consider in turn stellar mass binaries, extreme- and intermediate-mass ratio inspirals (EMRIs/IMRIs, respectively), and the coalescence of massive BHs.

1. Stellar mass binaries

Many stellar mass binaries involving neutron stars are expected to be eccentric in the LISA band (see e.g. [34]). It is also well known that LISA should provide a large observational sample of interacting white-dwarf binaries, whose evolution is driven by radiation reaction, tides and mass transfer [73]. It was recently realized that eccentric double white dwarfs formed in globular clusters would be detectable by LISA out to the Large Magellanic Cloud [74]. In these binaries, the periastron precession has contributions due to general relativity, but also to tidal and rotational distortions. Tides and stellar rotation should dominate at frequencies above a few megahertz. The Fisher-matrix analysis of [75] pointed out the interesting possibility to study white-dwarf structure with LISA. However their analysis neglected the contribution of radiation-reaction effects, that should be relevant for $f \gtrsim 0.5$ mHz. We expect our post-circular formalism to be useful in this context, since radiation reaction in these eccentric binaries should be well modeled by the quadrupole approximation.

2. Extreme- and intermediate-mass ratio inspirals

Formation scenarios for EMRIs and IMRIs, involving a SMBH and either a compact stellar mass object or an IMBH, are reviewed in Ref. [76]. If an EMRI is formed following a tidal binary separation event, the compact star is deposited on an orbit with semimajor axis $\simeq 10^2$–10^3 AU and $e \simeq 0.9$–0.99, and the orbit should circularize by the time it enters the LISA band. However, typical EMRIs are expected to form by scattering of the

compact object into nearly radial orbits followed by inspiral due to dissipation, and, in particular, due to GW emission. Hopman and Alexander [77] showed that the eccentricity distribution of EMRIs is skewed to high-e values, with a peak at $e \simeq 0.7$, at an orbital period of $\simeq 10^4$ s. The dynamical evolution of IMBH binaries formed in dense stellar clusters, using a combination of N-body simulations and three-body relativistic scattering experiments, shows that the eccentricity of these systems in the LISA band can be as large as $\simeq 0.2$–0.3 [78]. The post-circular approximation developed here could be applied to these systems once PN corrections are taken into account.

3. Massive black hole coalescence

The eccentricity of SMBH binaries has been the subject of some debate. Gravitational radiation reaction alone is not sufficient to produce mergers between massive BHs, which probably require dynamical interactions. Analytic calculations and N-body simulations show that, in purely collisionless spherical backgrounds, the expected equilibrium distribution of eccentricities is skewed towards high $e \simeq 0.6$–0.7, and that dynamical friction does not play a major role in modifying such a distribution (see Ref. [79], in particular, Fig. 5). The actual eccentricity of a merger event is therefore determined by the competition between dynamical wandering and GW-induced circularization. Reference [76] presents arguments supporting circularization of most binaries by the time they enter the LISA band. However, several mechanisms producing nonzero eccentricity have been proposed in the past (see e.g. Sec. 2 of Ref. [80]).

Recent smoothed-particle hydrodynamics simulations follow the dynamics of two BHs orbiting in massive, rotationally supported circumnuclear disks [81,82]. The rotation of the disk circularizes the orbit if the pair *corotates* with the disk. Circularization is efficient until the BHs bind in a binary, though in the latest stages of the simulations (when the separation is of the order of a few parsecs) a residual eccentricity $e \gtrsim 0.1$ is still present. Circularization possibly reduces the gravitational radiation merging time scale so much that the binary stalls, and no coalescence results. For corotating disks, the numerical resolution of the simulations is not sufficient to compute the residual eccentricity when the BHs are close enough that gravitational radiation takes over. Moreover, if the orbit of the pair is *counterrotating*, the initial eccentricity does not decrease, and BHs may enter the GW-dominated phase with high eccentricity.

Collisional processes (such as three-body encounters with background stars) may become important at BH separations $\lesssim 6$ pc, possibly leading to an increase in eccentricity balancing the circularization driven by the large-scale action of the gaseous and/or stellar disk. Several investigations show that eccentricity evolution may still occur in later stages of the binary's life, because of close encounters with single stars [83] and/or gas-dynamical processes [84]. In particular, the gravitational interaction of the binary with a surrounding gas disk is likely to excite BH binaries to eccentricities $e \gtrsim 0.1$. The transition between disk-driven and gravitational wave-driven inspiral can occur at small enough radii that a small but significant eccentricity survives, with typical values $e \simeq 0.02$ (and a lower limit of $e \simeq 0.01$) 1 yr prior to merger (cf. Fig. 5 of [84]). If the binary has an extreme mass ratio $q \lesssim 0.02$, the residual eccentricity can be considerably larger ($e \gtrsim 0.1$). Recent simulations by Cuadra *et al.* [85] investigate the evolution of the orbital parameters of binaries embedded within geometrically thin gas disks. For binary masses $10^5 M_\odot \lesssim M \lesssim 10^8 M_\odot$, they find that orbital decay due to gas disks may dominate the binary dynamics for separations below $a \simeq 10^{-1}$–0.1 pc, and that in the process the eccentricity grows at a rate $de/dt \simeq 1.5 \times 10^{-4} \omega_{\rm orb}$, where $\omega_{\rm orb}$ is the orbital frequency. Saturation of the eccentricity growth is not observed up to values $e \gtrsim 0.35$, so the binary may have significant eccentricity by the time gravitational radiation takes over.

Stellar dynamical hardening might also leave the binary with nonzero eccentricity. Early studies suggested that any such eccentricity would be small [83,86,87] (but see [88,89] for examples of eccentricity growth in N-body simulations). More recent N-body simulations combined with a Fokker-Planck model [90] find that perturbations of the (initially circular) binary orbit from passing stars produce significant eccentricity around or even before the time when the binary becomes hard. The averaged eccentricity growth is maximum for equal-mass binaries with $e \approx 0.75$ and falls to zero at $e = 0$ and $e = 1$. It is hard to estimate the final eccentricity, which strongly depends on noise-induced changes in e at early times, and would presumably be much smaller than the simulations suggest in the large-N regime of real galaxies.

Berentzen *et al.* [47] present simulations following the SMBH evolution in rotating galactic nuclei from kiloparsec separations down to coalescence, including PN corrections to the binary equations of motion. They find that the orbital eccentricities remain large (between 0.4 and 0.99, with typical values around $e \simeq 0.9$) until shortly before coalescence, and that higher harmonics of the eccentric signal are detectable by LISA with large SNR. Most of these binaries have sizable eccentricities (up to $\simeq 0.2$) by the time they reach a separation $\simeq 10^2$ Schwarzschild radii, which roughly corresponds to a binary of mass $M \approx 2 \times 10^6 M_\odot$ entering the LISA band (see e.g. Fig. 8 of [47]). The study by Sesana, Haardt, and Madau [91–93] confirms that binaries with mass ratio $q = M_2/M_1 \lesssim 0.1$ and/or eccentricity $e \gtrsim 0.3$ can shrink to the GW-dominated regime within a Hubble time (see, in particular, Fig. 7 of [92]; Sec. 4.1 and Fig. 10 of [93]). Last but not least, an interesting scenario producing highly eccentric mergers that could

be observed by LISA involves close *triple* SMBH encounters [94,95].

APPENDIX B: HIGHER-ORDER COEFFICIENTS

In this appendix we list some of the higher-order coefficients appearing in the expansion (3.6).

$$C_+^{(2)} = s_i^2\left(e^2 - \frac{1}{3}e^4 + \frac{1}{24}e^6 - \frac{1}{360}e^8\right) + (1 + c_i^2)c_{2\beta} \times \left(2 - 5e^2 + \frac{11}{4}e^4 - \frac{179}{360}e^6 + \frac{7}{160}e^8\right), \quad \text{(B1)}$$

$$C_+^{(3)} = s_i^2\left(\frac{9}{8}e^3 - \frac{81}{128}e^5 + \frac{729}{5120}e^7\right) + (1 + c_i^2)c_{2\beta} \times \left(\frac{9}{2}e - \frac{171}{16}e^3 + \frac{9477}{1280}e^5 - \frac{2187}{1024}e^7\right), \quad \text{(B2)}$$

$$C_+^{(4)} = s_i^2\left(\frac{4}{3}e^4 - \frac{16}{15}e^6 + \frac{16}{45}e^8\right) + (1 + c_i^2)c_{2\beta} \times \left(8e^2 - 20e^4 + \frac{752}{45}e^6 - \frac{688}{105}e^8\right), \quad \text{(B3)}$$

$$C_+^{(5)} = s_i^2\left(\frac{625}{384}e^5 - \frac{15\,625}{9216}e^7\right) + (1 + c_i^2)c_{2\beta} \times \left(\frac{625}{48}e^3 - \frac{26\,875}{768}e^5 + \frac{734\,375}{21\,504}e^7\right), \quad \text{(B4)}$$

$$C_+^{(6)} = s_i^2\left(\frac{81}{40}e^6 - \frac{729}{280}e^8\right) + (1 + c_i^2)c_{2\beta} \times \left(\frac{81}{4}e^4 - \frac{2349}{40}e^6 + \frac{146\,529}{2240}e^8\right), \quad \text{(B5)}$$

$$C_+^{(7)} = s_i^2\frac{117\,649}{46\,080}e^7 + (1 + c_i^2)c_{2\beta} \times \left(\frac{117\,649}{3840}e^5 - \frac{588\,245}{6144}e^7\right), \quad \text{(B6)}$$

$$C_+^{(8)} = s_i^2\frac{1024}{315}e^8 + (1 + c_i^2)c_{2\beta}\left(\frac{2048}{45}e^6 - \frac{48\,128}{315}e^8\right), \quad \text{(B7)}$$

$$C_+^{(9)} = (1 + c_i^2)c_{2\beta}\frac{4\,782\,969}{71\,680}e^7, \quad \text{(B8)}$$

$$C_+^{(10)} = (1 + c_i^2)c_{2\beta}\frac{390\,625}{4032}e^8, \quad \text{(B9)}$$

$$S_+^{(2)} = s_{2\beta}(1 + c_i^2)\left(2 - 5e^2 + 3e^4 - \frac{73}{180}e^6 + \frac{299}{2880}e^8\right), \quad \text{(B10)}$$

$$S_+^{(3)} = s_{2\beta}(1 + c_i^2)\left(\frac{9}{2}e - \frac{171}{16}e^3 + \frac{9783}{1280}e^5 - \frac{531}{256}e^7\right), \quad \text{(B11)}$$

$$S_+^{(4)} = s_{2\beta}(1 + c_i^2)\left(8e^2 - 20e^4 + \frac{763}{45}e^6 - \frac{4111}{630}e^8\right), \quad \text{(B12)}$$

$$S_+^{(5)} = s_{2\beta}(1 + c_i^2)\left(\frac{625}{48}e^3 - \frac{26875}{768}e^5 + \frac{23\,125}{672}e^7\right), \quad \text{(B13)}$$

$$S_+^{(6)} = s_{2\beta}(1 + c_i^2)\left(\frac{81}{4}e^4 - \frac{2349}{40}e^6 + \frac{147\,177}{2240}e^8\right), \quad \text{(B14)}$$

$$S_+^{(7)} = s_{2\beta}(1 + c_i^2)\left(\frac{117\,649}{3840}e^5 - \frac{588\,245}{6144}e^7\right), \quad \text{(B15)}$$

$$S_+^{(8)} = s_{2\beta}(1 + c_i^2)\left(\frac{2048}{45}e^6 - \frac{48\,128}{315}e^8\right), \quad \text{(B16)}$$

$$S_+^{(9)} = s_{2\beta}(1 + c_i^2)\frac{4\,782\,969}{71\,680}e^7, \quad \text{(B17)}$$

$$S_+^{(10)} = s_{2\beta}(1 + c_i^2)\frac{390\,625}{4032}e^8. \quad \text{(B18)}$$

$$C_\times^{(2)} = s_{2\beta}c_i\left(-4 + 10e^2 - \frac{11}{2}e^4 + \frac{179}{180}e^6 - \frac{7}{80}e^8\right), \quad \text{(B19)}$$

$$C_\times^{(3)} = s_{2\beta}c_i\left(-9e + \frac{171}{8}e^3 - \frac{9477}{640}e^5 + \frac{2187}{512}e^7\right), \quad \text{(B20)}$$

$$C_\times^{(4)} = s_{2\beta}c_i\left(-16e^2 + 40e^4 - \frac{1504}{45}e^6 + \frac{1376}{105}e^8\right), \quad \text{(B21)}$$

$$C_\times^{(5)} = s_{2\beta}c_i\left(-\frac{625}{24}e^3 + \frac{26\,875}{384}e^5 - \frac{734\,375}{10\,752}e^7\right), \quad \text{(B22)}$$

$$C_\times^{(6)} = s_{2\beta}c_i\left(-\frac{81}{2}e^4 + \frac{2349}{20}e^6 - \frac{146\,529}{1120}e^8\right), \quad \text{(B23)}$$

$$C_\times^{(7)} = s_{2\beta}c_i\left(-\frac{117\,649}{1920}e^5 + \frac{588\,245}{3072}e^7\right), \quad \text{(B24)}$$

$$C_\times^{(8)} = s_{2\beta}c_i\left(-\frac{4096}{45}e^6 + \frac{96\,256}{315}e^8\right), \quad \text{(B25)}$$

$$C_\times^{(9)} = -s_{2\beta}c_i\frac{4\,782\,969}{35\,840}e^7, \tag{B26}$$

$$C_\times^{(10)} = -s_{2\beta}c_i\frac{390\,625}{2016}e^8, \tag{B27}$$

$$S_\times^{(2)} = c_{2\beta}c_i\left(4 - 10e^2 + 6e^4 - \frac{73}{90}e^6 + \frac{299}{1440}e^8\right), \tag{B28}$$

$$S_\times^{(3)} = c_{2\beta}c_i\left(9e - \frac{171}{8}e^3 + \frac{9783}{640}e^5 - \frac{531}{128}e^7\right), \tag{B29}$$

$$S_\times^{(4)} = c_{2\beta}c_i\left(16e^2 - 40e^4 + \frac{1526}{45}e^6 - \frac{4111}{315}e^8\right), \tag{B30}$$

$$S_\times^{(5)} = c_{2\beta}c_i\left(\frac{625}{24}e^3 - \frac{26\,875}{384}e^5 + \frac{23\,125}{336}e^7\right), \tag{B31}$$

$$S_\times^{(6)} = c_{2\beta}c_i\left(\frac{81}{2}e^4 - \frac{2349}{20}e^6 + \frac{147\,177}{1120}e^8\right), \tag{B32}$$

$$S_\times^{(7)} = c_{2\beta}c_i\left(\frac{117\,649}{1920}e^5 - \frac{588\,245}{3072}e^7\right), \tag{B33}$$

$$S_\times^{(8)} = c_{2\beta}c_i\left(\frac{4096}{45}e^6 - \frac{96\,256}{315}e^8\right), \tag{B34}$$

$$S_\times^{(9)} = c_{2\beta}c_i\frac{4\,782\,969}{35\,840}e^7, \tag{B35}$$

$$S_\times^{(10)} = c_{2\beta}c_i\frac{390\,625}{2016}e^8. \tag{B36}$$

APPENDIX C: THE ξ_k COEFFICIENTS

The coefficients defined in Eq. (4.31) are given by the following expressions, when one fixes $\beta = \iota = 0$:

$$\begin{aligned}
\xi_1 &= -\Big[\Big(-\frac{19\,496\,441}{368\,640}F_+ - \frac{20\,671\,709}{368\,640}iF_\times\Big)e^7 \\
&\quad + \Big(\frac{111\,701}{4608}F_+ + \frac{119\,365}{4608}iF_\times\Big)e^5 \\
&\quad + \Big(-\frac{535}{48}F_+ - \frac{563}{48}iF_\times\Big)e^3 + 3(F_+ + iF_\times)e\Big], \\
\xi_2 &= \Big(\frac{17\,653\,698\,319}{53\,084\,160}iF_\times + \frac{17\,504\,123\,791}{53\,084\,160}F_+\Big)e^8 \\
&\quad + \Big(-\frac{40\,020\,301}{276\,480}iF_\times - \frac{39\,618\,829}{276\,480}F_+\Big)e^6 \\
&\quad + \Big(\frac{8267}{128}F_+ + \frac{8331}{128}iF_\times\Big)e^4 + \frac{277}{12}(-F_+ - iF_\times)e^2 \\
&\quad + 4(F_+ + iF_\times), \\
\xi_3 &= \Big(-\frac{39\,934\,951}{122\,880}F_+ - \frac{40\,111\,999}{122\,880}iF_\times\Big)e^7 \\
&\quad + \Big(\frac{368\,823}{2560}F_+ + \frac{370\,047}{2560}iF_\times\Big)e^5 \\
&\quad + \frac{813}{16}(-F_+ - iF_\times)e^3 + 9(F_+ + iF_\times)e, \\
\xi_4 &= \Big(-\frac{6\,662\,759}{10\,752}F_+ - \frac{300\,571\,739}{483\,840}iF_\times\Big)e^8 \\
&\quad + \Big(\frac{389\,167}{1440}iF_\times + \frac{388\,463}{1440}F_+\Big)e^6 \\
&\quad + \frac{277}{3}(-F_+ - iF_\times)e^4 + 16(F_+ + iF_\times)e^2, \\
\xi_5 &= \frac{13\,445\,625}{28\,672}(F_+ + iF_\times)e^7 - \frac{89\,375}{576}(iF_\times + F_+)e^5 \\
&\quad + \frac{625}{24}(F_+ + iF_\times)e^3, \\
\xi_6 &= \Big(\frac{5\,605\,821}{7168}F_+ + \frac{28\,049\,841}{35\,840}iF_\times\Big)e^8 \\
&\quad - \frac{39\,987}{160}(F_+ + iF_\times)e^6 + \frac{81}{2}(F_+ + iF_\times)e^4, \\
\xi_7 &= -\frac{117\,649}{92\,160}(-48 + 307e^2)e^5(F_+ + iF_\times), \\
\xi_8 &= -\frac{256}{945}(-336 + 2227e^2)e^6(F_+ + iF_\times), \\
\xi_9 &= \frac{4\,782\,969}{35\,840}e^7(F_+ + iF_\times), \\
\xi_{10} &= \frac{390\,625}{2016}e^8(F_+ + iF_\times).
\end{aligned} \tag{C1}$$

APPENDIX D: ENDING FREQUENCY FOR ECCENTRIC BINARIES

In this appendix we discuss possible generalizations of the notion of an ISCO to eccentric binaries. The idea is that eccentric binaries will transition from inspiral to plunge at a frequency slightly different from the circular ISCO fre-

quency, and we may worry about the effect of this modified ISCO on the upper cutoff frequency used in SNR calculations.

A possible way to modify the ISCO location is to use the Newtonian formula in Eq. (2.4) with $a = p/(1-e^2)$ and $p = 6+2e$, which corresponds to the value of the separatrix between stable and unstable (plunging) orbits. In this way we would find that the ISCO frequency is

$$F_{\rm ISCO} = \frac{1}{2\pi M}\left(\frac{1-e^2}{6+2e}\right)^{3/2}. \tag{D1}$$

This guess cannot be valid for large eccentricities, when the pericenter becomes small, since then the Newtonian relations break down. A more accurate approximation of the ISCO frequency is to use the pericenter frequency $\Omega_p^2 = M/r_p^3$ at the separatrix pericenter $r_p = 6+2e$, leading to [96–98]

$$F_{\rm ISCO} = \frac{1}{2\pi M}\left(\frac{1+e}{6+2e}\right)^{3/2}, \tag{D2}$$

but this result is also not appropriate here because this eccentricity corresponds to that associated with Schwarzschild geodesics, so it is not equivalent to the Newtonian definition of eccentricity we have used (see e.g. [69] for a discussion).

One expects the residual eccentricity any binary could have by the time it enters the strong field to be small. The classic work of Peters and Mathews [8] and Peters [9] suggests that a binary with some moderate initial eccentricity will rapidly circularize. Since $e/e_0 \sim (f/f_0)^{-19/18}$ to leading order [see e.g. Eq. (2.34) in [10]], an orbit with initial eccentricity $e_0 = 0.4$ at the beginning of the LIGO band will have a final eccentricity of $e \simeq 0.035$ by the time it reaches LIGO's highest sensitivity region at 200 Hz. These results suggest that the ISCO frequency for eccentric inspirals will generically be close to the ISCO frequency for circular inspirals, provided this frequency is much larger than the initial frequency associated with the initial eccentricity. If the latter is not the case (e.g. if a binary with $e_0 = 0.4$ at $F_0 = 20$ Hz merges at 40 Hz), then one might have to worry about the precise definition of the ISCO, but in such cases the SNR will be dominated by the merger waveform and not the inspiral. We are thus justified to ignore eccentric corrections to the ISCO and employ the usual circular-orbit ISCO expression in our SNR calculations.

APPENDIX E: FREQUENCY AT A GIVEN TIME BEFORE MERGER

LISA sources can easily orbit for more than 1 yr in the LISA band. The LISA mission, however, is not expected to last for more than a few years in orbit. For this reason, it is customary to perform LISA SNR and parameter estimation calculations assuming that the source is observed over the last year (or few years) of inspiral.

In the case of circular inspirals, one can compute exactly (to Newtonian order) the frequency at a given time T prior to merger. This is given by Eq. (2.15) in Ref. [65]:

$$f_{\rm yr} = 4.149\times 10^{-5}\left(\frac{\mathcal{M}}{10^6 M_\odot}\right)^{-5/8}\left(\frac{T}{1\ {\rm yr}}\right)^{-3/8}\ {\rm Hz}. \tag{E1}$$

This equation can be obtained by finding $T(F)$ as the integral of $\dot{F}^{-1}$ and then inverting the resulting expression to find $F(T)$.

In the case of eccentric inspirals, an analogous relation cannot be obtained analytically. This is because the equation for $\dot{F}$ in Eq. (4.24) is a function of the eccentricity, which itself is a function of the frequency (and implicitly time). One could attempt to construct an approximation for $F(T)$ by inserting Eq. (3.11) for $e(F)$ into the expression for $\dot{F}$ in Eq. (4.24) to compute $T(F)$, and then perturbatively inverting this relation to find $F(T)$. The resulting asymptotic series, however, is poorly convergent for large masses or large integration times.

A numerical procedure is thus necessary to find $f_{\rm yr}$ for eccentric inspirals. One such scheme is as follows. Given some e_0 and F_0, one can find the corresponding initial semimajor axis a_0 from the first equality in Eq. (2.4). From this, one can then use this same equation to find the corresponding constant c_0. The eccentricity e_T a time T before merger is then given by Eq. (5.14) in [8], namely,

$$T(a_0, e_0) = \frac{12}{19}\frac{c_0^4}{\beta}\int_0^{e_T}\frac{dee^{29/19}}{(1-e^2)^{3/2}}\left(1+\frac{121}{304}e^2\right)^{1181/2299}, \tag{E2}$$

where $\beta = m_1 m_2 M$. This is because the eccentricity at zero orbital separation (roughly corresponding to "merger") vanishes in the Newtonian approximation. If

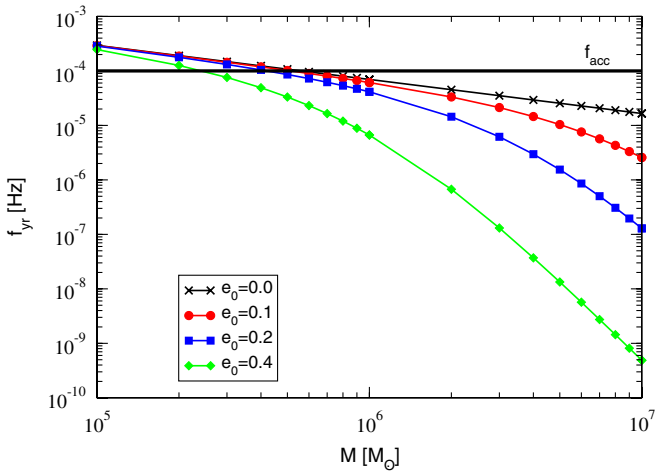

FIG. 9 (color online). Frequency 1 yr prior to merger as a function of total mass for equal-mass binaries with different initial eccentricity: $e_0 = 0$ (crosses), $e_0 = 0.1$ (circles), $e_0 = 0.2$ (squares), and $e_0 = 0.4$ (diamonds). The quantity $f = 10^{-4}$ Hz corresponds to the acceleration noise cutoff frequency.

we set $T = 1$ yr, then we can solve Eq. (E2) for $e_{\rm yr}$ numerically using bisection or the secant method in MATHEMATICA. Once the appropriate $e_{\rm yr}$ is found, one can use this to find $a_{\rm yr}$ via Eq. (2.4), which can then also be used to find $f_{\rm yr}$ for some given e_0 and M.

Figure 9 plots the dominant GW frequency (twice the orbital frequency) 1 yr prior to merger found with the above algorithm as a function of total mass for equal-mass binaries with different initial eccentricities. Observe that as the eccentricity increases, $f_{\rm yr}$ decreases faster with total mass than in the circular case, because eccentricity speeds up the inspiral. Thus, given a fixed inspiral time (e.g. 1 yr), the starting frequency must be pushed to lower values. Care must be taken, however, since $f_{\rm yr}$ appears multiplied by $\ell/2$ in the step functions used to truncate the waveform. Nonetheless, the above figure suggests that for total masses $M \gtrsim 10^6 M_\odot$ it does not matter whether one uses the circular or eccentric expressions for $f_{\rm yr}$.

[1] B. S. Sathyaprakash and B. F. Schutz, Living Rev. Relativity **12**, 2 (2009).
[2] LIGO, http://www.ligo.caltech.edu/.
[3] VIRGO, http://www.virgo.infn.it/.
[4] GEO600, http://www.geo600.uni-hannover.de/.
[5] TAMA, http://tamago.mtk.nao.ac.jp/.
[6] LISA, http://lisa.jpl.nasa.gov/.
[7] http://www.et-gw.eu/.
[8] P. C. Peters and J. Mathews, Phys. Rev. **131**, 435 (1963).
[9] P. C. Peters, Phys. Rev. **136**, B1224 (1964).
[10] T. Mora and C. M. Will, Phys. Rev. D **69**, 104021 (2004).
[11] L. Wen, Astrophys. J. **598**, 419 (2003).
[12] R. M. O'Leary, B. Kocsis, and A. Loeb, Astrophys. J. **395**, 2127 (2009).
[13] P. Peters and J. Mathews, Phys. Rev. **131**, 435 (1963).
[14] R. Wagoner and C. Will, Astrophys. J. **210**, 764 (1976).
[15] L. Blanchet and G. Schäfer, Mon. Not. R. Astron. Soc. **239**, 845 (1989).
[16] L. Blanchet and G. Schäfer, Classical Quantum Gravity **10**, 2699 (1993).
[17] R. Rieth and G. Schäfer, Classical Quantum Gravity **14**, 2357 (1997).
[18] A. Gopakumar and B. R. Iyer, Phys. Rev. D **56**, 7708 (1997).
[19] K. G. Arun, L. Blanchet, B. R. Iyer, and M. S. S. Qusailah, Phys. Rev. D **77**, 064034 (2008).
[20] K. G. Arun, L. Blanchet, B. R. Iyer, and M. S. S. Qusailah, Phys. Rev. D **77**, 064035 (2008).
[21] K. G. Arun, L. Blanchet, B. R. Iyer, and S. Sinha, arXiv:0908.3854.
[22] L. Blanchet, T. Damour, B. R. Iyer, C. M. Will, and A. G. Wiseman, Phys. Rev. Lett. **74**, 3515 (1995).
[23] L. Blanchet, G. Faye, B. R. Iyer, and B. Joguet, Phys. Rev. D **65**, 061501(R) (2002); **71**, 129902(E) (2005).
[24] L. Blanchet, T. Damour, G. Esposito-Farèse, and B. R. Iyer, Phys. Rev. Lett. **93**, 091101 (2004).
[25] L. Blanchet, B. R. Iyer, C. M. Will, and A. G. Wiseman, Classical Quantum Gravity **13**, 575 (1996).
[26] K. G. Arun, L. Blanchet, B. R. Iyer, and M. S. S. Qusailah, Classical Quantum Gravity **21**, 3771 (2004); **22**, 3115(E) (2005).
[27] L. E. Kidder, L. Blanchet, and B. R. Iyer, Classical Quantum Gravity **24**, 5307 (2007).
[28] L. Blanchet, G. Faye, B. R. Iyer, and S. Sinha, Classical Quantum Gravity **25**, 165003 (2008).
[29] T. Damour, A. Gopakumar, and B. R. Iyer, Phys. Rev. D **70**, 064028 (2004).
[30] C. Konigsdorffer and A. Gopakumar, Phys. Rev. D **73**, 124012 (2006).
[31] K. Martel and E. Poisson, Phys. Rev. D **60**, 124008 (1999).
[32] N. Seto, Phys. Rev. Lett. **87**, 251101 (2001).
[33] M. Benacquista, arXiv:astro-ph/0106086.
[34] M. J. Benacquista, Living Rev. Relativity **5**, 2 (2002).
[35] M. Tessmer and A. Gopakumar, Phys. Rev. D **78**, 084029 (2008).
[36] T. Cokelaer and D. Pathak, Classical Quantum Gravity **26**, 045013 (2009).
[37] A. Krolak, K. D. Kokkotas, and G. Schäfer, Phys. Rev. D **52**, 2089 (1995).
[38] C. Moreno-Garrido, J. Buitrago, and E. Mediavilla, Mon. Not. R. Astron. Soc. **266**, 16 (1994).
[39] C. Moreno-Garrido, E. Mediavilla, and J. Buitrago, Mon. Not. R. Astron. Soc. **274**, 115 (1995).
[40] V. Pierro, I. M. Pinto, A. D. Spallicci, E. Laserra, and F. Recano, Mon. Not. R. Astron. Soc. **325**, 358 (2001).
[41] V. Pierro, I. M. Pinto, and A. D. A. M. Spallicci, Mon. Not. R. Astron. Soc. **334**, 855 (2002).
[42] C. Van Den Broeck and A. Sengupta, Classical Quantum Gravity **24**, 155 (2007).
[43] K. G. Arun, B. R. Iyer, B. S. Sathyaprakash, and S. Sinha, Phys. Rev. D **75**, 124002 (2007).
[44] K. S. Thorne, in *Three Hundred Years of Gravitation*, edited by S. Hawking and W. Israel (Cambridge University Press, Cambridge, England, 1987), pp. 330–458.
[45] M. Trias and A. M. Sintes, Phys. Rev. D **77**, 024030 (2008).
[46] B. Vaishnav *et al.*, Classical Quantum Gravity (to be published).
[47] I. Berentzen, M. Preto, P. Berczik, D. Merritt, and R. Spurzem, Astrophys. J. **695**, 455 (2009).
[48] C. W. Misner, K. Thorne, and J. A. Wheeler, *Gravitation* (W. H. Freeman & Co., San Francisco, 1973).
[49] H. Goldstein, C. Pool, and J. Safko, *Classical Mechanics* (Addison-Wesley, Reading, MA, 2000).
[50] A. Gopakumar and B. R. Iyer, Phys. Rev. D **65**, 084011 (2002).
[51] M. Abramowitz and A. Stegun, *Handbook of Mathematical Functions* (Dover Publications, New York, 1970).
[52] T. A. Apostolatos, Phys. Rev. D **52**, 605 (1995).

[53] H. Wahlquist, Gen. Relativ. Gravit. **19**, 1101 (1987).
[54] C. M. Bender and S. A. Orszag, *Advanced Mathematical Methods for Scientists and Engineers I: Asymptotic Methods and Perturbation Theory* (Springer-Verlag, Berlin, 1999).
[55] C. Cutler and E. E. Flanagan, Phys. Rev. D **49**, 2658 (1994).
[56] S. Droz, D. J. Knapp, E. Poisson, and B. J. Owen, Phys. Rev. D **59**, 124016 (1999).
[57] A. M. Sintes and A. Vecchio, in *Rencontres de Moriond: Gravitational Waves and Experimental Gravity*, edited by J. Dumarchez (Frontières, Paris, 2000).
[58] A. M. Sintes and A. Vecchio, in *Third Amaldi Conference on Gravitational Waves*, edited by S. Meshkov, AIP Conf. Ser. No. 523 (AIP, New York, 2000), p. 403.
[59] T. A. Moore and R. W. Hellings, Phys. Rev. D **65**, 062001 (2002).
[60] R. W. Hellings and T. A. Moore, Classical Quantum Gravity **20**, S181 (2003).
[61] C. Van Den Broeck and A. S. Sengupta, Classical Quantum Gravity **24**, 1089 (2007).
[62] K. G. Arun, B. R. Iyer, B. S. Sathyaprakash, S. Sinha, and C. V. D. Broeck, Phys. Rev. D **76**, 104016 (2007).
[63] E. K. Porter and N. J. Cornish, Phys. Rev. D **78**, 064005 (2008).
[64] K. G. Arun, A. Buonanno, G. Faye, and E. Ochsner, Phys. Rev. D **79**, 104023 (2009).
[65] E. Berti, A. Buonanno, and C. M. Will, Phys. Rev. D **71**, 084025 (2005).
[66] K. G. Arun, B. R. Iyer, B. S. Sathyaprakash, and P. A. Sundararajan, Phys. Rev. D **71**, 084008 (2005); **72**, 069903(E) (2005).
[67] https://workarea.et-gw.eu/et/WG4-Astrophysics/base-sensitivity/wg4-assumptions.pdf.
[68] C. Cutler, Phys. Rev. D **57**, 7089 (1998).
[69] U. Sperhake *et al.*, Phys. Rev. D **78**, 064069 (2008).
[70] I. Hinder, F. Herrmann, P. Laguna, and D. Shoemaker, arXiv:0806.1037.
[71] M. Favata (private communication).
[72] B. Kocsis *et al.* (private communication).
[73] A. Stroeer, A. Vecchio, and G. Nelemans, Astrophys. J. **633**, L33 (2005).
[74] B. Willems, A. Vecchio, and V. Kalogera, Phys. Rev. Lett. **100**, 041102 (2008).
[75] B. Willems *et al.*, Astrophys. J. **665**, L59 (2007).
[76] P. Amaro-Seoane *et al.*, Classical Quantum Gravity **24**, R113 (2007).
[77] C. Hopman and T. Alexander, Astrophys. J. **629**, 362 (2005).
[78] P. Amaro-Seoane, C. Miller, and M. Freitag, Astrophys. J. **692**, L50 (2009).
[79] M. Colpi, L. Mayer, and F. Governato, Astrophys. J. **525**, 720 (1999).
[80] E. Berti, Classical Quantum Gravity **23**, S785 (2006).
[81] M. Dotti, M. Colpi, and F. Haardt, Mon. Not. R. Astron. Soc. **367**, 103 (2006).
[82] M. Dotti, M. Colpi, F. Haardt, and L. Mayer, Mon. Not. R. Astron. Soc. **379**, 956 (2007).
[83] P. Berczik, D. Merritt, R. Spurzem, and H.-P. Bischof, Astrophys. J. **642**, L21 (2006).
[84] P. J. Armitage and P. Natarajan, Astrophys. J. **634**, 921 (2005).
[85] J. Cuadra, P. J. Armitage, R. D. Alexander, and M. C. Begelman, Mon. Not. R. Astron. Soc. **393**, 1423 (2009).
[86] G. D. Quinlan, arXiv:astro-ph/9601092.
[87] G. D. Quinlan and L. Hernquist, arXiv:astro-ph/9706298.
[88] T. Matsubayashi, H. Shinkai, and T. Ebisuzaki, Astrophys. J. **614**, 864 (2004).
[89] S. J. Aarseth, Astrophys. Space Sci. **285**, 367 (2003).
[90] D. Merritt, S. Mikkola, and A. Szell, Astrophys. J. **671**, 53 (2007).
[91] A. Sesana, F. Haardt, and P. Madau, Astrophys. J. **651**, 392 (2006).
[92] A. Sesana, F. Haardt, and P. Madau, Astrophys. J. **660**, 546 (2007).
[93] A. Sesana, F. Haardt, and P. Madau, Astrophys. J. **686**, 432 (2008).
[94] L. Hoffman and A. Loeb, Mon. Not. R. Astron. Soc. **377**, 957 (2007).
[95] M. Iwasawa, Y. Funato, and J. Makino, arXiv:0801.0859.
[96] C. Cutler, D. Kennefick, and E. Poisson, Phys. Rev. D **50**, 3816 (1994).
[97] J. Levin and G. Perez-Giz, Phys. Rev. D **79**, 124013 (2009).
[98] P. G. Komorowski, S. R. Valluri, and M. Houde, Classical Quantum Gravity **26**, 085001 (2009).